Die approbierte Originalversion dieser Diplom-/Masterarbeit ist in der Hauptbibliothek der Technischen Universität Wien aufgestellt und zugänglich.
http://www.ub.tuwien.ac.at

The approved original version of this diploma or master thesis is available at the main library of the Vienna University of Technology.
http://www.ub.tuwien.ac.at/eng

TECHNISCHE UNIVERSITÄT WIEN
Vienna University of Technology

DIPLOMA THESIS

Thermal conductivity of nitride based thin films

carried out for the purpose of obtaining the degree Master of Science
under supervision of

Univ.Prof. Dipl.-Ing. Dr.mont. Paul Heinz Mayrhofer

E 308 - Institute of Material Science and Technology
special field Material Science

submitted at

Vienna University of Technology
Getreidemarkt 9/164-CT
1060 Wien

by

Vincent MORAES
0726207
Brunnengasse 39/20, 1160 Wien

Vienna, 31st of March, 2015

This work was supported by Plansee Composite Materials GmbH and
Oerlikon Balzers Surface Solutions AG in the framework of the Christian Doppler
Laboratory
for Application Oriented Coating Development.

Affidavit:
I declare in lieu of oath, that I wrote this thesis and performed the associated research myself, using only literature cited in this volume.

Date *Signature*

Acknowledgements

First of all I want to thank my supervisor **Univ.Prof. Dipl.-Ing. Dr.mont. Paul Heinz Mayrhofer** for giving me the opportunity to accomplish this study in the framework of the Christian Doppler Laboratory for Application Oriented Coating Development. Despite his tight time schedule, he always found a sympathetic ear for all my more or less challenging questions.

Furthermore I am very grateful to my thesis supervisor and long-time friend DI **Helmut Riedl**. He spared no effort to support me with all the challenging tasks and showed patience whenever things were not easy. I am also grateful to all my colleagues within the Thin Film Group for all the support and all the fun I had while working on this thesis.

Last but not least I want to thank **my whole family** and notably the most important person in my life for all their support. **Anna**, you always listened to all my problems and found encouraging words to give me a moral uplift.

Contents

Contents iv

Abstract 1

1 Introduction 4

2 Thermal conductivity in solid matter 6

2.1 Introduction . . . 6

2.2 High thermal conductive materials . . . 9

2.2.1 Diamond . . . 11

2.2.2 Silicon Carbide . . . 12

2.2.3 Aluminum Nitride . . . 12

3 Thermal conductivity - measurement methods 14

3.1 Heated suspended bar technique . . . 15

3.2 Laser flash diffusivity . . . 16

3.3 3-omega method . . . 16

4 Deposition and growth 21

4.1 Physical Vapor Deposition (PVD) . . . 21

4.2 Chemical Vapor Deposition (CVD) . . . 24

4.3 Thin film growth . . . 25

5 Analysis **27**

5.1 X-Ray Diffraction (XRD) 27

5.2 Hardness measurement - Nanointentation 27

5.3 Scanning Electron Microscopy (SEM) 28

5.4 Profilometer 30

Bibliography **31**

Publication I **35**

Abstract

Abstract

An increasing demand on thermal protective coatings as well as high thermal conductive thin films has led to a huge variety of nitride based thin films for various thermal management applications. On one side of the scale are wurtzite aluminum nitride thin films, a representative of the III-V semiconductors, which have drawn great attention over the last decades due to its extremely high thermal ($\kappa \sim 320\,\mathrm{W \cdot m^{-1} \cdot K^{-1}}$ [1]) and rather low electrical conductivity (band gap of about 6 eV). In addition, an excellent thermal stability recommends AlN as an attractive material for electronic packaging applications. On the other side of the scale are cubic titanium and chromium nitride-based thin films ($\kappa \sim 4.8\,\mathrm{W \cdot m^{-1} \cdot K^{-1}}$ [2]). Their outstanding properties such as high hardness and thermal stability as well as low friction behavior make them ideal for the use as protective coatings in forming and tooling applications.

Within this study, we investigated the influence of the alloying content on the temperature dependent thermal conductivity in Ti-, Al-, and CrN based coatings. Therefore, a PVD reactive magnetron sputtering system was applied to deposit TiN, $Ti_{1-x}Al_xN$, AlN, $Al_{1-x}Cr_xN$ and CrN thin films. The morphology, the crystal structure, as well as the mechanical properties of the sputtered thin films were investigated applying XRD, SEM, TEM, and nanoindentation analysis. For determination of the thermal conductivity the 3-omega method was applied. This measurement technique requires high thermal conductive substrate materials, which were found in 100 oriented Si wafers ($\kappa \sim 142.5\,\mathrm{W \cdot m^{-1} \cdot K^{-1}}$ [3]). To extend the measuring range, the differential operation mode of the 3ω method had to be carried out. Simulations of the thermal conductivity measurements predicts, that the used setup is limited to a measureable thermal conductivity of $\sim 50\,\mathrm{W \cdot m^{-1} \cdot K^{-1}}$, which is clearly exceeded by our AlN thin films. The measurements, especially for the high thermal conductive AlN, show great sensitivity to the heater widths, which were applied via lithography.

Doping small amounts of 10 at.% chromium on the metal sublattice of the AlN thin films

has no effect on the single phased wurtzite structure, which is also obtained for pure AlN. Although the similar crystal structure and morphology, the 3ω measurement reveals a great drop in the thermal conductivity compared to pure AlN. These impurities or point defects have serious impact on the phonon mobility, which are the major carrier of the thermal conductivity in insulating materials. The effect of alloying Al in TiN is not that pronounced. The transition metal nitride (TiN, CrN) coatings exhibit higher thermal conductivity as their bulk counterparts, which is mainly based on the high point defect density due to the PVD process.

The results show the possibility of designing coatings with perfectly defined thermal conductivity (e.g., by the alloying concepts as proven for our binary nitrides alloyed with Al) and reveal the importance of the crystal structure for the thermal conductivity. Furthermore, we clearly pointed out the importance of the purity of a material to show its unique properties.

Kurzfassung

Eine gezielte Wärmeabfuhr bzw. Wärmeverteilung spielt in vielen industriellen Anwendungen und Produkten eine immer größer werdende Rolle. Sei es eine Anwendung, wie die einer Wendeschneidplatte, deren Einsatz eine niedrige thermische Leitfähigkeit an der Oberfläche verlangt um das Werkzeug vor zu hohen Temperaturen zu schützen, oder die Wärmeabfuhr elektronischer Bauteile einer Platine, welche den Einsatz von Materialien mit hoher Wärmeleitfähigkeit verlangt. Um dabei den Einsatz aufwendiger Kühlsysteme zu vermeiden, können nitrid-basierende Schichtsysteme einen großen Fortschritt im Temperaturmanagement bedeuten. Aluminiumnitrid, ein Vertreter aus der Gruppe der III-V Halbleiter, das durch die Kombination einer extrem hohen thermischen Leitfähigkeit ($\kappa \sim 320\,\mathrm{W \cdot m^{-1} \cdot K^{-1}}$ [1]) und einer niedrigen elektrischen Leitfähigkeit (Bandlücke von ca. 6 eV) besticht, eignet sich auch aufgrund seiner hohen thermischen Stabilität für die Anwendung in elektronischen Bauteilen und Platinen. Dem entgegen stehen Ti- und CrN basierende Schichten ($\kappa \sim 4.8\,\mathrm{W \cdot m^{-1} \cdot K^{-1}}$ [2]), die meist für Anwendungen mit thermischen Barrieren verwendet werden. Deren hohe Härte und thermische Stabilität, sowie ausgezeichnete Reibeigenschaften sind ideale Voraussetzungen für den Einsatz in der Bearbeitungsindustrie (z.B Zerspanung und Formgebung).

Das Ziel dieser Arbeit war die Untersuchung des Einflusses von Legierungselementen (Al, Cr) auf die temperaturabhängige thermische Leitfähigkeit von TiN, AlN und CrN basierender Schichten. Dazu wurden mit Hilfe der plasmaunterstützten reaktiven Magnetronkathoden-Zerstäubung (sputtern) verschiedene TiN, $\mathrm{Ti_{1-x}Al_xN}$, AlN, $\mathrm{Al_{1-x}Cr_xN}$ und CrN Schichten abgeschieden. Es wurden XRD, REM, TEM und Nanoindentation Analysen durchgeführt um die Morphologie, Kristallstruktur und mechanischen Eigenschaften der Schichten zu untersuchen. Zur Ermittlung der temperaturabhäng-

igen thermischen Leitfähigkeit wurde die 3ω Methode angewandt. Um die thermische Leitfähigkeit von hochleitfähigen Schichten mittels der 3ω Methode bestimmen zu können, bedarf es Substratmaterialen mit einem weitaus höheren κ . Für diese Studie wurden daher 100 orientierte Si Wafer Substrate ($\kappa \sim 142.5\,\mathrm{W \cdot m^{-1} {\cdot} K^{-1}}$ [3]) verwendet und die 3ω Methode wurde im differentiellen Messmodus verwendet. Die Simulationen der Messergebnisse weisen auf ein oberes Auflösungslimit von $\sim 50\,\mathrm{W \cdot m^{-1} {\cdot} K^{-1}}$ hin. Dieses Messlimit wurde aufgrund der hohen thermischen Leitfähigkeit der AlN Schichten erreicht und überschritten. Weiters zeigte die Messung eine sehr hohe Empfindlichkeit gegenüber der Breite der photolithographisch aufgebrachten Metallheizer.

Durch die Dotierung von 10 at.% Cr ins Metalluntergitter der AlN Schichten, kam es unter Beibehaltung der Wurtzit-Struktur und Schichtmorphologie zu einem Einbruch der thermischen Leitfähigkeit. Diese Punktdefekte nehmen großen Einfluss auf die Ausbreitung der Majoritätsträger der Wärme in isolierenden Materialien, den sogenannten Phononen. Der unerwartete Anstieg der thermischen Leitfähigkeit mit steigender Temperatur (im betrachteten Temperaturfenster) konnte auf das mit dem PVD-Prozess einhergehende Einbringen von hohen Punktdefektdichten zurückgeführt werden.

Die Ergebnisse dieser Studie zeigen die Möglichkeit, durch die Dotierung von Schichtsystemen, gezielt die thermische Leitfähigkeit zu kotrollieren. Des Weiteren wurde die Abhängigkeit der thermischen Eigenschaften von der Kristallstruktur, Morphologie und der Reinheit der Materialien gezeigt.

Chapter 1

Introduction

The historical evolution of human cultures is strongly related to the availability of raw material resources. This circumstances are revealed by naming whole periods by their prevailing materials. In course of time, the improvement of tools and materials by combining various elements has always been a major driving force in the progress of mankind. However, to fulfill the modern technical demands, the requirements on material properties became increasingly challenging [4].

Nowadays, material scientists and engineers face, besides the optimization of the material properties, many different challenges. The choice of material has to be in balance with the availability, reduced costs, convenience and last but not least, the environmental concerns. To fulfill these outstanding challenges, the simple improvement of the bulk material is no longer sufficient [5]. The modification of the surface by thin films offers enormous potential to improve the functionality of existing products and create entirely new and revolutionary products. Furthermore, it combines the desired properties of the bulk material with the adjustable properties of coatings.

A well established process for the deposition of thin films is the Physical Vapor Deposition (PVD) process in which a material is vaporized from a solid or liquid source and transported to the surface of a substrate where it condenses. Due to the fact that there are no solubility restrictions in the vapor phase for atomic, ionic or molecular species, the deposition technique allows the preparation of multi-component materials over an extended range of compositions compared to bulk materials. Consequently, thin films span a huge range of applications in fields of tooling, optics, electronics, aero-space engineering, and other industries [6].

The thermal properties of thin films become more and more important due to their influences in the thermal management in various applications. The coating can either act as a thermal barrier (when obtaining low thermal conductivity) or help in eliminating hot spots by obtaining a high thermal conductivity. Therefore, the enormous range of thermal (and other)

properties of nitride based coatings such as TiN, AlN, or CrN, have draw great attention to the scientific community and the industry [7].

Considering the importance of the crystal structure, the possibility of alloying nitride based coatings in PVD processes can lead to an improvement of different properties. Therefore improvements have been made in alloying Al in the industrially well established TiN and CrN coatings. Scaling with the Al content, tremendous effects such as age hardening and an improved oxidation resistance (e.g., for $Ti_{1-x}Al_xN$) or thermal stability (e.g., for $Al_{1-x}Cr_xN$) have been observed. In addition, this offers new possibilities by modifying the resulting new coatings. State of the art coating development already yields to quasi ternary alloys such as $Al_{1-x-y}Cr_xTM_yN$, doping transition metals (TM) or other elements such as Si, C or O into ternary systems. For instance, the oxidation resistance of $Al_{1-x}Cr_xN$ coatings can be improved by alloying small amounts of oxygen active elements such as yttrium [8].

The goal of the present study was to analyze the influence of the alloying content (Al and Cr) on the temperature dependent thermal conductivity of nitride based thin films (TiN, AlN, and CrN) using the 3ω method. To get a deeper understanding on the thermal conductivity of the coatings, the results were related to their crystal structure, morphology, and deposition conditions coupled with investigations on the mechanical properties of the coatings.

Chapter 2

Thermal conductivity in solid matter

2.1 Introduction

In solids, heat energy can be transmitted via electrical carriers (electrons or holes), lattice waves (phonons), spin waves or electromagnetic waves [9, 10]. For instance in metals, the majority of the heat is carried by the free electron gas, while in insulators the dominant heat transfer is provided by phonons. Therefore, the total thermal conductivity, κ, can be determined as the sum of all components representing the different excitations [11].

In addition, the micro-structure of solid materials plays an important role for their thermal conductivity. Material properties such as the grain size, the number of lattice defects or imperfections, the dislocation density as well as anharmonicity of the lattice forces and carrier concentrations, essentially influences the thermal conductivity.

In general the thermal conductivity is defined as

$$\kappa = -\frac{\overrightarrow{Q}}{\overrightarrow{\nabla} T}. \quad (2.1)$$

In equation 2.1, T is the absolute temperature and $\overrightarrow{Q}$ the heat flux vector across a unit cross section perpendicular to $\overrightarrow{Q}$. The negative sign indicates the flow of heat from the hot to the cold end.

As already mentioned above, the thermal conductivity in metals is dominated by free electrons. Therefore, we use the line of thought from the kinetic theory of gases. Considering a metal bar with a cold and a hot end, a temperature gradient exists and the electrons in the hot end pick up this energy and start traveling to the cold end. To maintain charge neutrality, an equal number of electrons must travel from the hot to the cold and vice versa, hence the transported heat is proportional to the difference in the energy of the electrons (see Figure 2.1) [12].

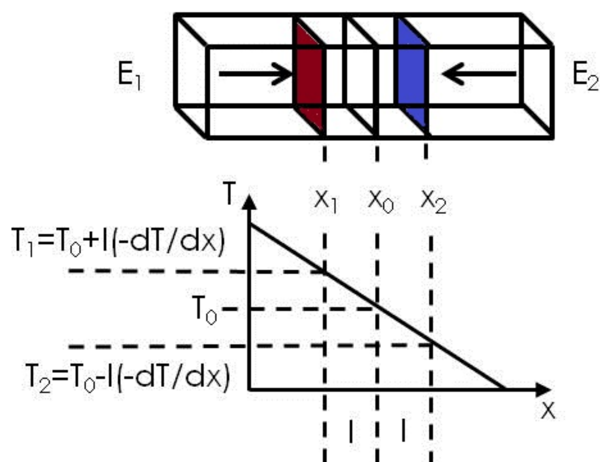

Figure 2.1: Heat conductivity in metals [12].

Under this considerations, the heat conductivity of the electrons is determined by

$$\kappa = \frac{n_v \nu k_B l}{2} \tag{2.2}$$

As one can see from equation 2.2, the thermal conductivity increases with the number of electrons (n_v) that are involved, with the mean free path between the collisions (l), and with increasing the velocity (ν). In equation 2.2, k_B is the Boltzmann constant.

Wiedemann and Franz [13] observed, that materials which are good electrical conductors are also good thermal conductors. They came to the conclusion, that the ratio of the electrical conductivity (σ) and the thermal conductivity (κ) are proportional to the product of a constant value (the so called the Lorentz number 2.1-2.9$\cdot 10^{-4}$ W $\cdot$ $\Omega\cdot$K^{-2}) and the temperature. Their empirical law (see equation 2.3) is especially valid for metals.

$$\frac{\sigma}{\kappa} = LT \tag{2.3}$$

In Table 2.1 the electrical and thermal conductivity values of typical metals are listed.

Table 2.1: Electrical and thermal conductivity of selected metals [14].

Element	σ**[S/m] at 300K**	κ **[W/cmK] at 300K**
aluminum	$3.66\cdot 10^7$	2.37
copper	$5.80\cdot 10^7$	4.01
gold	$4.40\cdot 10^7$	3.17
silver	$6.14\cdot 10^7$	4.29
iron	$1.00\cdot 10^7$	0.80

Due to the lack of free electrons in nonmetals, heat conduction is executed by a different mechanism. In crystalline matter, atoms vibrate around their equilibrium positions due to the uptake of thermal energy, and these vibrations are strongly coupled to their neighboring atoms. The quanta of the atomic vibrational modes postulated by Einstein [12], the so called phonons, have wave-particle duality and can be seen as elastic waves propagating in either longitudinal and/or transversal direction. In analogy with electrons, the properties of phonons can be described by density of state curves as well as band diagrams (see Figure 2.2). In terms of band diagrams the branches have sinusoidal character, hence they are not longer called valence or conduction bands rather than acoustic and optical bands due to their frequencies. The main difference of phonons compared to electrons is, that phonons are not conserved but are created by raising temperature and eliminated by lowering it.

For a hypothetically infinite large, isotropically pure single-crystal with no imperfections, the thermal conductivity at all temperatures (where phonons are existent), is infinite, which means that phonons of a single-crystal would carry all the heat from the hot end to the cold end. But as real crystals are of finite size and contain all kinds of defects, the lifetime of a phonon and subsequently the thermal conductivity is finite.

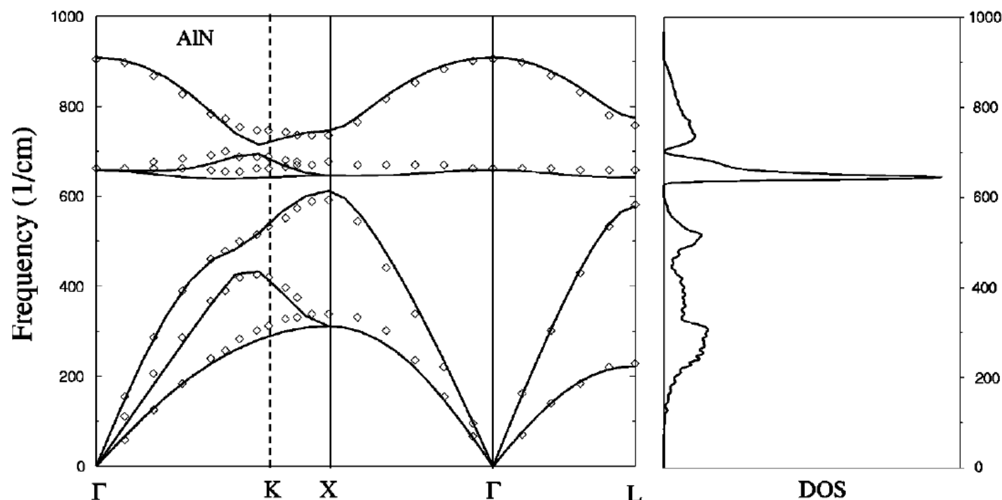

Figure 2.2: Phonon-dispersion curves and density of states of AlN in the zinc blende structure (β-AlN) [15].

As it was discussed in means on the thermal conductivity of metals, the common approach for the understanding of the thermal conductivity in crystalline dielectric materials is based on the equation for heat transfer in gases (see Eq. 2.2). Therefore the lattice vibrations of the crystal are treated as a gas of phonons,

$$\kappa = \frac{1}{3}\nu\lambda C^{ph}, \tag{2.4}$$

In equation 2.4, ν is the mean phonon group velocity, λ the mean free path of the phonons between collisions and C^{ph} is the heat capacity per unit volume. Phonons from the optical branches are ineffective heat carriers due to their small group velocity, but can attenuate the heat flux by interacting with acoustic phonons. The heat capacity is represented by three acoustic modes and 3n-3 optic modes, where n is the number of atoms per unit cell [12].

As already mentioned, the drifting phonons interact on their path with external boundaries, imperfections and other phonons. These interactions result in a limitation of the phonon lifetime and furthermore in an alteration of phonon frequencies and momenta. This can be seen as thermal resistivity analogous to the electrical resistivity of electrons. At low temperatures where only a few phonons are present, the thermal conductivity mainly depends on the heat capacity. The main sources of their scattering are boundary scattering, scattering from point imperfections or stacking faults. At higher temperatures respectively higher phonon density, the mean free path decreases, and so phonon-phonon interactions become increasingly important.

Phonon-phonon interactions can be seperated into four-phonon and three-phonon processes. Four-phonon processes are in general two to three orders of magnitude weaker in strength than three-phonon processes and shall not be further discussed. A classification of three-phonon processes separates it into class 1 and class 2 processes. For a class 1 phonon process, a phonon interacts with a second phonon creating a third phonon, fulfilling the law of energy and quasi-momentum conservation. On the other hand, in a class 2 process a phonon decays into two phonons of less energy. Both processes can either take place in a normal or an Umklapp manner. For a normal process the momentum sum of the phonons has to be confined to the first Brillouin zone. This zone describes a uniquely defined primitive cell in the reciprocal space of a crystal. However, in an Umklapp process, the momentum sum lies beyond the first zone and requires a flip back with the help of a reciprocal lattice vector [15, 16].

2.2 High thermal conductive materials

Over the last few centuries, thermal management of mechanical, chemical and electrical systems became more and more important. Therefore, either low or high thermal conductive materials get into focus for miscellaneous applications. Metals are known to be good thermal conductors. For instance, copper is most commonly used when high thermal and great electrical conductivity is required. But using it for thermal management in electronic applications, the as good electrical conduction occurs as an insuperable problem due to insulation requirements. Besides the electrical conduction, the high density, subsequently high weight, as well as the high coefficient of thermal expansion makes most of the metals unsuitable for several applications. In this section, the structural requirements for high thermal conductive

ceramics, which are suitable for electronic packaging will be discussed.

In general, ceramics are either insulating or semi-conductive materials. The electrical conductance of a material depends on the band gap between the valence and the conduction band. Within electrically insulating materials, the thermal conductivity can span an enormously wide range. From diamond, which disposes a thermal conductivity up to $2200\,\mathrm{W \cdot m^{-1} \cdot K^{-1}}$ [17], to amorphous solids in the range of $10^{-4}\,\mathrm{W \cdot m^{-1} \cdot K^{-1}}$. To obtain high thermal conductivity, there are three criteria which are of fundamental importance in the heat transport in a lattice [15, 18, 19].

- **Debye temperature**
  The debye frequency, ω_D, is defined as the maximum vibrational frequency of a given (acoustic or optic) mode. In case of the more interesting acoustic mode, it corresponds to the frequency in the Brillouin zone. Therefore one can define a Debye temperature, θ_a which can be understood as the lower limit, above all vibrational modes are excited (see equation 2.5).
  $$\theta_a = \frac{\hbar \omega_D}{k_B}, \tag{2.5}$$
  where $\hbar$ represents the Planck constant and k_B the Boltzmann constant. So each branch will have a defined Debye temperature in the three dimensional case. Possessing a high Debye temperature is fundamental for high thermal conductivity.

- **Grueneisen parameter**
  The Grueneisen parameter is defined as the rate of change of the vibrational frequency ω_i of a given mode with volume V
  $$\gamma = -\frac{d \ln \omega_i}{d \ln V}, \tag{2.6}$$
  and is a measure for the departure of a crystal from its harmonicity. A small Grueneisen parameter is needed for high thermal conductive materials.

- **Crystal structure**
  With the increasing number of atoms, n, the size of the unit cell respectively the lattice constant increases and hence the Brillouin zone decreases. This means, that the Brillouin zone boundary is shifted towards smaller values of the phonon frequency. Therefore, a smaller number of atoms in the unit cell leads to theoretically higher thermal conductivity.

In Table 2.2, some of the most common representatives of miscellaneous structures are given.

Table 2.2: Calculated and experimental thermal conductivity values of selected compounds at room temperature [15].

Compound	θ_a [K]	γ [1]	δ [Å]	κ_{calc} $[\frac{W}{cmK}]$	κ_{exp} $[\frac{W}{cmK}]$	**Crystal structure**
NaCl	220	1.56	2.81	0.05	0.07	rocksalt
KCl	172	1.45	3.14	0.04	0.07	(n=2)
MgO	600	1.44	2.11	0.60	0.60	(B1)
CaO	450	1.57	2.40	0.33	0.27	
C	1450	0.75	1.78	16.40	30.00	zincblende/
Si	395	1.06	2.71	1.71	1.66	diamond
BN	1200	0.70	1.81	11.05	7.60	(n=2)
GaAs	220	0.75	2.83	0.55	0.45	(B3/A4)
SiC	740	0.75	2.18	4.45	4.90	wurtzite
AlN	620	0.70	2.18	3.03	3.50	(n=4)
GaN	390	0.70	2.25	1.59	2.10	(B4)
ZnO	303	0.75	2.29	0.65	0.60	

2.2.1 Diamond

Carbon crystallizes in two different modifications, the so called allotropes, diamond and graphite. In the cubic structure of a diamond (A4) every carbon atom is tetrahedral bonded (sp^3 hybrid orbitals) to four other carbon atoms (see Figure 2.3). Because of the high

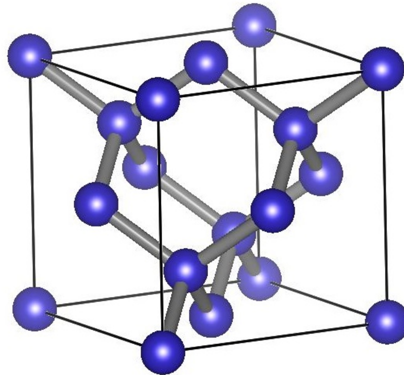

Figure 2.3: Diamond structure (A4).

binding energy (covalent bonds), diamond obtains great hardness for which it is often used in drilling or cutting applications. The wide indirect band gap of 5.5eV, which results in high electrical resistivity and an outstanding thermal conductance ($\kappa \sim 2200\,\mathrm{W} \cdot \mathrm{m}^{-1} \cdot \mathrm{K}^{-1}$ [17]) made it an interesting material for several applications. Diamond is metastable and changes

its modification above 1500°C, under the exclusion of oxygen, into the more stable graphite modification [20].

Since 1955, diamond can be synthesized by high-pressure synthesis [21]. In the 80's, a new way of synthesizing diamond and diamond films was developed, the chemical vapor deposition (CVD). Therefore, gaseous carbohydrates get cracked down into radicals and fragments which deposit on heated substrates as metastable polycrystalline diamond films. Nowadays, numerous variations of this method exists. CVD processed diamond films provide theoretically dense, polycrystalline material of high purity. Under optimized growth conditions it exhibits many mechanical, electrical and thermal properties comparable to natural diamond.

2.2.2 Silicon Carbide

Silicon carbide appears to be one of the hardest material with excellent resistance to chemical and thermal influences. It forms tetrahedral covalent bonds and occurs in different modifications. One of this modifications crystallizes in the zincblende (B3) structure, which is very similar to the structure of diamond. For commercial use, silicon carbide is synthesized either by the Acheson method, where silica sand and graphite form α-SiC (hexagonal or rhomboidal structure), or the thermal decomposition of methylchlorsilanes, which forms β-SiC (cubic structure).
Nowadays, SiC in all different varieties can be synthesized by CVD as well as physical vapor deposition processes (PVD) depending on the deposition requirements. Because of its low price and excellent thermal and mechanical properties, silicon carbide is often used as abrasive material or disks for brakes. In literature, the thermal conductivity is reported to be $490\,\mathrm{W}\cdot\mathrm{m}^{-1}\cdot\mathrm{K}^{-1}$ [20, 22, 23].

2.2.3 Aluminum Nitride

The wide, direct band gap (6.2eV) and the great thermal conductivity makes AlN an attractive material for electronic packaging applications. Furthermore, its great piezoelectric properties may be suitable for the application in surface acoustic wave devices. AlN also exhibits excellent mechanical and thermal properties, which makes it desirable for many applications. Due to the high affinity of aluminum towards oxygen, the formation of high quality AlN requires high purity source material (Al) and an oxygen free environment.
Aluminum nitride is known to crystallize in the hexagonal wurtzite structure (B4) (see Figure 2.4) at ambient pressure conditions. The unit cell is represented by four atoms which are tetrahedrally coordinated. The lattice constants are a_w=3.11 Å and c_w=4.98 Å [24] and AlN has partially covalent as well as ionic bonds. At higher pressures, aluminum nitride shows a phase transition into the rocksalt phase (B1) starting at a pressure of 14 GPa and com-

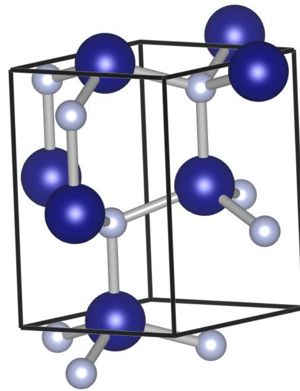

Figure 2.4: Wurtzite structure (B4).

pleting at 20 GPa. The rocksalt structure persists when the pressure is released to ambient conditions [25].

As already mentioned, AlN is highly reactive to oxygen. The diffusion of 1 wt.% oxygen into the specimen is reported to decrease the thermal conductivity from its bulk (single crystal) value of $300\,\mathrm{W \cdot m^{-1} {\cdot} K^{-1}}$ to $71\,\mathrm{W \cdot m^{-1} {\cdot} K^{-1}}$ [15]. For sintered AlN, this problem has been limited by effective sintering aids, oxygen trapping into grains, and firing under a reducing (e.g N_2) atmosphere. Because of the partially covalent bonds, it is difficult to densify AlN. Further problems for the decreasing of thermal conductance could occur due to random orientation of the grains or secondary phases with poor conductivities at the grain boundaries. Cai et al. pointed out, that annealing is an efficient way to improve the thermal conductivity [26].

For the synthesis of aluminum nitride thin films, a huge variety of different methods, such as plasma enhanced chemical vapor deposition (PE-CVD), atomic layer deposition (ALD), molecular beam epitaxy (MBE), and AC/DC (magnetron sputtering), could be used [27].

Chapter 3

Thermal conductivity - measurement methods

Accurate determination of the thermal conductivity of solids can pose many challenges, due to several loss terms of the heat input, which has to be considered and quantified. There is a great variety of different measurement methods, each having their own advantages as well as their inherent limitations. They reach from the direct measurement of the thermal conductivity to indirect measurements and calculation via the thermal diffusivity. Furthermore, the techniques differ on various heating and temperature sensing methods such as electrical and optical ones or the combination of both.

When it comes to thin films, the characterization of the thermal conductivity gets even more challenging. Large numbers of potential defects, a change in micro-structure and as well the geometry due to the fabrication processes often leads to a more or less variance and anistropicity of thermal properties compared to bulk materials. Additionally, the substrate plays an important role. For example - if you want to determine the cross-plane thermal conductivity, the arising difficulty is to create and detect a reasonable temperature drop across the film without creating a large temperature rise in the substrate. Furthermore, the temperature at the interface ($T_{interface}$) needs to be determined. On the other hand, the detection of a temperature drop in plane seems easy but the occurring heat leakage through the substrate makes it difficult to determine the actual heat flow (see Figure 3.1) [11]. To eliminate these difficulties, different strategies and achievements have been developed to determine the cross- and in-plane thermal conductivity of thin films. The method of choice depends on many considerations, such as the size and shape of the specimen and the required accuracy. Therefore, uncertainties of the thermal conductivity within the range of $\sim 5\%$ have been observed [28].

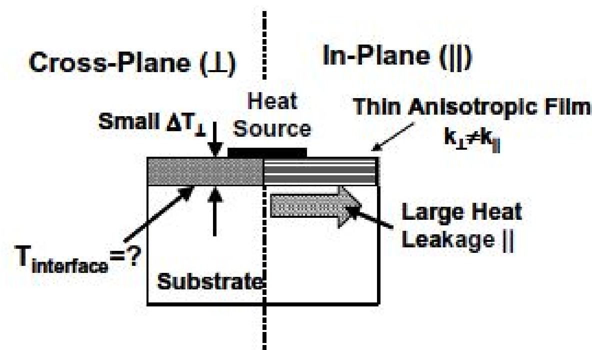

Figure 3.1: Sample configuration and characterization challenges [11].

3.1 Heated suspended bar technique

The heated suspended bar technique is an effective method for measuring the lateral thermal conductivity. One end of the specimen is attached to an isothermal heat sink at a defined temperature. At the other end, the specimen is equipped with a mostly deposited electrical heater. A row of thermocouples or resistive thermometers are fixed within a defined distance from the heater (and each other). Experimental errors, like the conduction through the heater wires, can be minimized by using thin wires. The heat loss accounted to the surface by molecular air conduction can be reduced by performing the whole experiment in vacuum. Furthermore the effect of surface radiation can be lowered by adding a second heater (see Figure 3.2). By knowing the dimensions of the specimen, the thermal conductivity can

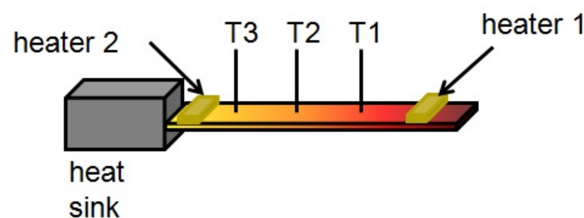

Figure 3.2: Schematics of a DC-heated suspended bar technique.

be directly determined via the thermal gradient. The advantages of this technique are the simplicity of the analysis and the high accuracy in the measurement of the thermal gradient. A disadvantage can be the labor-intensive (preparation of the heater, etc.) and slow procedure [29].

3.2 Laser flash diffusivity

This technique is based on optical heating. One face of the sample is exposed to a short ($\leq 1\ ms$) laser pulse. On the opposite side of the sample, an infrared (IR) thermometer monitors the temperature rise (see Figure 3.3).

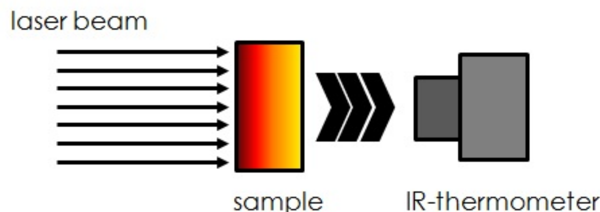

Figure 3.3: Schematics of the laser-flash diffusivity technique.

From the temperature rise versus time profile, the thermal diffusivity is calculated. The relation between the thermal diffusivity (D), and the thermal conductivity (κ) is shown in equation 3.1 where ρ represents the density and c_p the heat capacity under constant pressure.

$$D = \frac{\kappa}{\rho c_p} \tag{3.1}$$

At high temperatures, the heat capacity can be seen as constant, hence the measurement yields directly to the thermal conductivity. This technique requires a highly accurate setup in order to prevent "'flash-throughs"' to the IR detector. Furthermore, the sample surfaces have to be highly emissive to the IR radiation which can be obtained by a thin graphite layer on top. Several algorithms for determining and correcting the measurement specific various losses exist and need to be considered [30].

3.3 3-omega method

The 3-omega method (3-ω method), or often also called the Ångström technique, is a proper method to investigate the thermal conductivity of thin films. It overcomes the difficulties of black body irradiation by an increase of the effective thickness of the sample. This thickness increase minimizes the ratio of the surface for possible heat exchange to the surrounding media. Initially, it was developed for thermal conductivity measurements of bulk materials, but was later on extended for thermal characterization of thin films. Moreover, the method was extended to measure the in-plane respectively cross-plane thermal conductivity for anisotropic materials. For the 3-omega method a thin metal strip is deposited onto the surface of the sample as shown in Figure 3.4. The metal strip acts as a heater as well as a

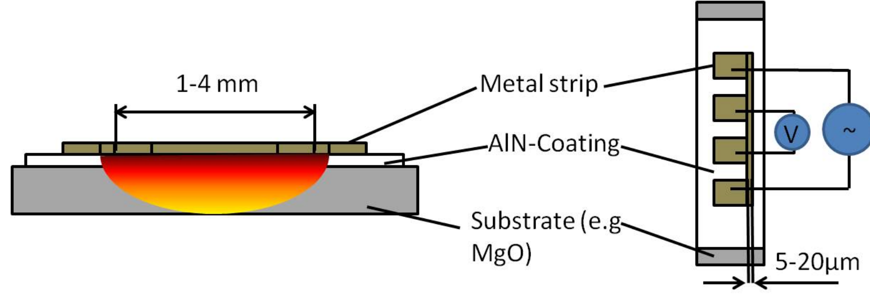

Figure 3.4: Shematics of the 3ω method.

temperature sensor. On the outer pads, an alternating current (AC), I(t), with an angular frequency, ω, and an amplitude, I_0, is applied,

$$I(t) = I_0 \cos(\omega t). \tag{3.2}$$

This generates a heating source with the power, P(t), where R_h represents the resistance of the metal strip (under experimental conditions),

$$P(t) = I_0^2 R_h \cos^2(\omega t) = \{\frac{I_0^2 R_h}{2}\}_{DC} + \{\frac{I_0^2 R_h \cos(\omega t)}{2}\}_{2\omega}, \tag{3.3}$$

and leads to a corresponding temperature rise of

$$T(t) = T_{DC} + T_{2\omega} \cos(2\omega + \varphi). \tag{3.4}$$

which contains a direct current (DC) term and a 2ω modulated AC component with a phase shift of φ. If the resistance of the heater has a linearly dependence on the temperature, the resistance also shows a 2ω variation.

$$\begin{aligned} R_h(t) &= R_0\{1 + C_{rt}\{T_{DC} + T_{2\omega} cos(2\omega t + \varphi)\}\} \\ &= R_0(1 + C_{rt}T_{DC})_{DC} + (R_0 C_{rt} T_{2\omega} \cos(2\omega t + \varphi))_{2\omega} \end{aligned} \tag{3.5}$$

In equation 3.5, R_0 is the heater resistance under no heating conditions and C_{rt} describes the temperature coefficient of the resistance for the metallic heater. By multiplying the applied AC current (equation 3.2) with the resistance (equation 3.5) the voltage drop, V(t), across the heater length can be calculated:

$$\begin{aligned} V(t) = I(t)R_h(t) = \{I_0 R_0(1 + C_{rt}T_{DC} \cos(\omega t)\}_{powersource} \\ +\{\frac{I_0 R_0 C_{rt} T_{2\omega}}{2} \cos(3\omega t + \varphi)\}_{3\omega mod} + \{\frac{I_0 R_0 C_{rt} T_{2\omega}}{2} \cos(3\omega t + \varphi)\}_{1\omega mod} \end{aligned} \tag{3.6}$$

By using a lock-in amplifier, the 3ω term, which is proportional to the temperature rise of the heater, is detectable and can be used to measure the temperature amplitude of the heater. The temperature rise of the heater is therefore obtained by varying the modulation

frequency of the current at a constant voltage. One of the occurring challenges of this technique is to measure the 3ω signal, which is typically about 3 orders of magnitude smaller than the applied voltage. In order to determine the temperature dependence of the thermal conductivity, this procedure can be repeated at the desired temperatures.

To use this technique for thin films, the heat conduction model used to obtain the substrate and thin film thermal conductivity, is of crucial importance. Mostly, a simplified model is applied using a line source for the heater, one-dimensional frequency independent heat conduction across the film, and a two dimensional heat transport in a semi-infinite substrate [31]. Under all these assumptions, the temperature amplitude (T_{S+F}) of the metal heater can be seen as

$$T_{S+F} = T_S + \frac{p}{l} \cdot \frac{t_f}{2bk_F}. \tag{3.7}$$

In equation 3.7, the ratio p/l is the power amplitude normed on the heater length, t_f represents the film thickness, k_F the cross-plane thermal conductivity of the film, b the half-width of the heater, and T_S the temperature rise at the film-substrate interface.
The measured temperature on the surface of the specimen contains the temperature drop across the film and the substrate. To determine the thermal conductivity of the thin film, one must know the temperature at the interface between the coating and the substrate. To solve this problem, there are two known approaches.
One approach to determine the temperature drop across a thin film, is to infer it experimentally, also called the differential technique. For this method the difference of the temperature rise between heaters deposited on the sample and a reference sample (see Figure 3.5), or an identical structured but thinner film is recorded. The film, respectively the difference in their thickness acts as a thermal barrier for the heat conduction through the substrate.

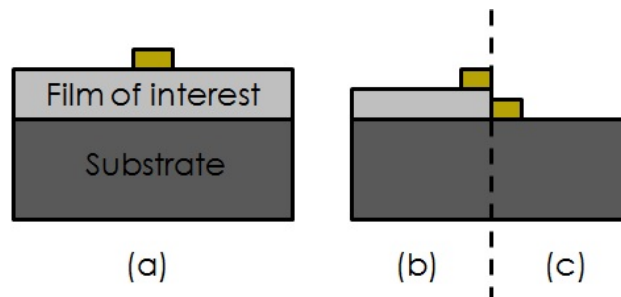

Figure 3.5: Sample requirement - differential technique: (a) specimen (b) reference sample, and (c) reference sample for an electrical insulating substrate.

The second approach is the calculation of the temperature rise at the film-substrate interface. Under the aspect of the line source approximation, the temperature rise of a semi-infinite bare substrate can been seen as

$$T_S = \frac{p}{\pi l k_s}\{0.5ln(\frac{\alpha_s}{b^2}) - 0.5ln(2\omega) + \eta\} - i\{\frac{p}{4lk_s}\}$$
$$= \frac{p}{\pi l k_s} f(ln(\omega)) \tag{3.8}$$

In equation 3.8, k_s represents the thermal conductivity and α_s the thermal diffusivity of the substrate. It becomes clear that when combining equation 3.7 and equation 3.8, the thermal conductivity of an isotropic substrate can be determined from the slope of the real part of the ac temperature amplitude as a function of $\ln(\omega)$. Nevertheless, the thermal conductivity of the thin film can be determined by using equation 3.9 (see Figure 3.6).

$$k_F = \frac{p}{l} \cdot \frac{t_f}{2b(T_{S+F} - T_S)} \tag{3.9}$$

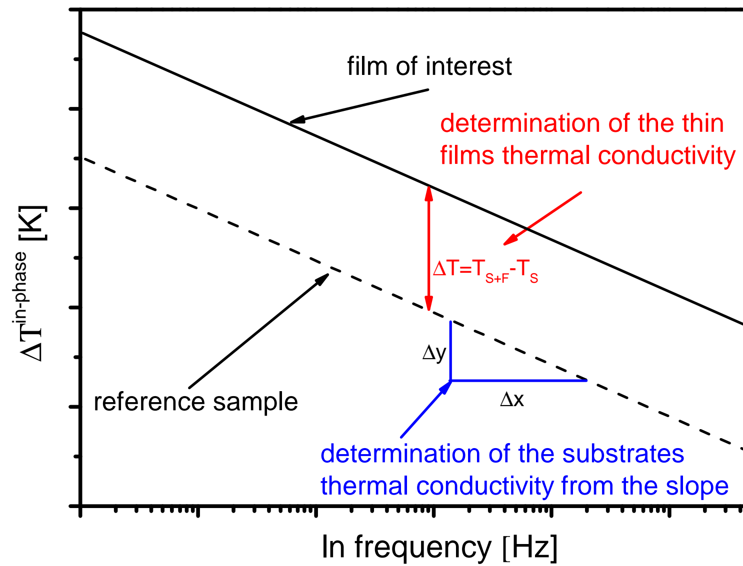

Figure 3.6: Schematics of the determination of the thermal conductivity from the 3-ω method.

For the determination of anisotropic thermal conductivities, the ratio of the heater width, b, and the film thickness, t_f, plays a key role. Using a strip width, smaller or comparable to the thickness of the film, it can be assumed that the measured temperature drop is more sensitive to the in-plane thermal conductivity. On the contrary, using a heater width much larger than the film thickness, the temperature rise is mainly sensitive to the cross-plane thermal conductivity (see Figure 3.7) [11, 15, 32–39].

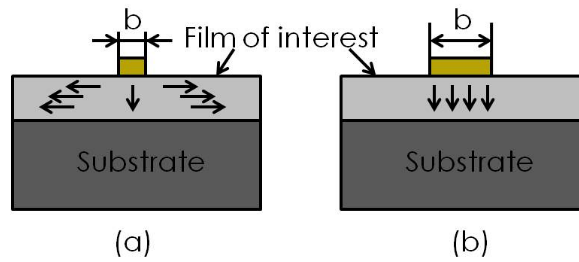

Figure 3.7: Experimental methods for anisotropic thermal conductivity (a) in plane (b) cross-plane.

CHAPTER 4

Deposition and growth

Due to their extensive applications in various fields of tooling, optics, electronics, space science, aircraft, defense and other industries, thin film science has become a fully-fledged discipline. The compactness, the low package weight and the mostly better performance combined with the possible reduced production cost, makes thin film components more attractive over their uncoated bulk counterparts. Besides their thickness, thin film properties are very sensitive to their structure which is strongly coupled to the production process and conditions, and the underlying material. In general the term "thin film" refers to layers less than one micron and may be as thin as a few atomic layers. Above one micron the films are often called coatings [40].
Usually, comparable bulk materials are sintered from powders with a few μm particle size. However, thin films are synthesized from ultra-fine particles such as atoms or clusters. Due to the fact that there are no solubility restrictions in the vapor phase for atomic, ionic or molecular species, the deposition techniques allow the preparation of metastable phases as well as multi-component materials over an extended range of compositions. This allows the preparation of phases often not accessible via other routes to form bulk materials. Depending on the application, each thin film process has its own advantages and disadvantages. Due to the use of various materials, different preparative techniques have been developed over the last few decades. In Figure 4.1, a general overview of well-established techniques is illustrated.

4.1 Physical Vapor Deposition (PVD)

In general, physical vapor deposition, is characterized as an atomistic deposition process. Therefore, a target material is vaporized from a solid or liquid source and transported through a vacuum or low pressure gaseous environment to a substrate (mostly, heated), where it condenses. Furthermore, the gaseous environment (e.g Nitrogen) can be used to form new

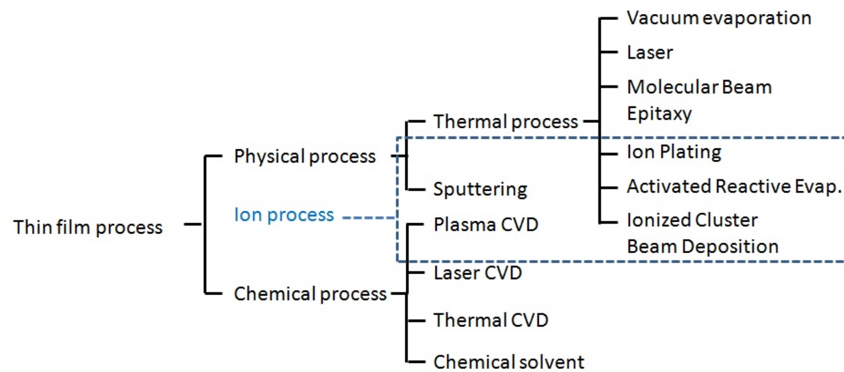

Figure 4.1: Overview of thin film deposition techniques [41].

compounds during the reaction with the vaporized target material. The distinction between different PVD processes is based on their vaporization technique, into an either thermal or sputtering processes. The method of choice is often based on the used target material.

The non-thermal sputtering process (see Figure 4.2a) is based on the principle of momentum transfer from atom-sized particles. In this technique, surface near atoms and clusters are ejected from a solid target material (cathode) through bombardment with accelerated ions, such as from argon or nitrogen. Depending on the energy of the impinging particles, several side effects like the reflection as a high energy neutral or implantation into the surface, can occur and furthermore affect the film formation process. About 95 % of the transferred energy appears as heat in the surface respectively near-surface region. The resulting sputtering yield (ratio of sputtered particles to the number of impinging particles) depends on various conditions such as the mass of the bombarding particle respectively its kinetic energy and the angle of incidence. The sputtered particles (atoms, clusters and ions) are then transferred to the substrate (very often also the anode) where they form a thin film via condensation.

The most common method of sputtering is plasma based sputtering. In general, a plasma is defined as a quasi-neutral (co-existence of ions and electrons) state of matter with collective behavior. It is generated through the collisions of electrons and atoms from the low pressure working gas. This results, depending on the I-V characteristics, in different zones of a discharge between the anode and the cathode which can be seen in Figure 4.2b. The sputtering methods can be seperated by the applied electrical field into Direct Current (DC), pulsed Direct Current (pulsed DC), Radio Frequency (RF), and ion beam sputtering. This modes allows the PVD process to be optimized in terms of the sputtering yield for given material systems.

In the DC diode configuration, a plasma is formed uniformly over a large area of the target material, so that a very smooth erosion can be realized. A problem in this configuration

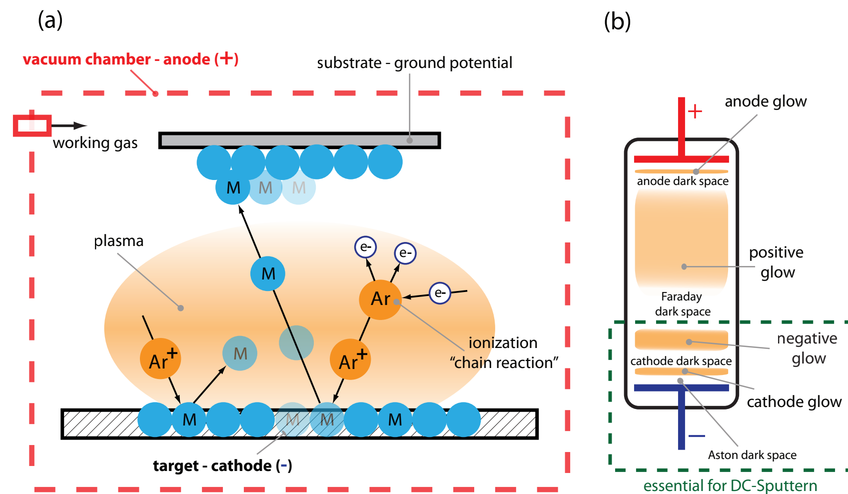

Figure 4.2: Schematics of the (a) sputtering process [42] (b) glow discharge [6].

is the very low deposition rate combined with rather high voltages. The electrons that are ejected from the cathode sustaining the discharge, are not efficiently used and lead to deductions of the plasma. This problem can be overcome, by arranging the cathode in a suitable magnetic field which forces the electrons to stay near the target surface. Thereby, the electrons can be trapped on closed trajectories resulting in increasing ionization of the working gas and an increase in the sputtering yield, respectively. The so called magnetron sputtering technique also maintains for far lower applied electrical voltages (from thousands to a few hundred volts). For enhancing the ion flux and consequently the film growth and density, an additional negative voltage to the substrate can be applied, the so called bias voltage. Thereby, positively charged ions are also attracted to the substrate (and hence growing film) to transfer their kinetic energy leading to activated film-forming. Moreover, a further energy input through substrate heating optimizes the film density. Another possibility to provide a source of energy for heating the substrates is to use not only negative but also positive bias - either DC, pulsed DC or RF signals. In case of an insulating substrate surface, RF is needed. The attracted flux of electrons can be used to heat the surface. Nevertheless, too high bias voltages (especially negative bias voltages) can also lead to the disadvantage of resputterting effects on the film surfaces [43]. As previously already mentioned, a suitable working gas can also be used to form new compounds via reactions with the species from the target material in a PVD process. The major disadvantage of this so called reactive sputtering technique is the possibility of forming insulating layers directly at the target surface (target poisoning). The resulting buildup of surface charges insulates the target material and can lead to arcing.

The most common technique used for insulating target materials, is radio frequency sputtering. The advantage of this technique is that during one part of the cycle, the ions are accelerated to the surface (causing sputtering), and in the second part the electrons can

reach the surface of the target to revers any charge buildup. To minimize the dielectric losses due to insulating targets, a metal electrode can be bonded underneath the target. The used frequencies range typically from 5 to 350 kHz. As a negative side effect, applying this technique leads to a decrease of the deposition rate, as only one half of the RF signal is used for sputtering.

Another technique for sputtering of dielectric matter is to apply a pulsed DC signal between the anode and the cathode. Adjusting certain pulsing frequencies and duty cycles, depsoitions with high growth rates and low possibility for arcing can be achieved.

The ion beam technique, uses a seperated chamber, where the ions are generated and further extracted into the sputtering chamber. The advantage is that this technique can be performed in high vacuum conditions and at high pumping speeds, which reduces the unintended contamination [44].

Due to the high kinetic energy of the arriving atoms on the substrate surface, sputtered thin films are able to reveal structures with increased defect densities, which leads to certain material properties [45]. In case of the thermal conductivity, an increased number of defects yields to enhanced scattering effects and hence reduced thermal conductivities compared to perfect crystals.

4.2 Chemical Vapor Deposition (CVD)

The chemical vapor deposition is an alternative to the physical vapor deposition technique. In addition to the applications mentioned in terms of PVD it is also used to produce high purity bulk materials as well as composite materials via infiltration techniques. A big advantage of CVD is, that the technique does not require as good vacuum conditions due to highly pure source compounds. Another advantage is the conformal film growth which allows the coating of elaborately shaped pieces, including all areas and undercuts. The big disadvantages are the restriction of the used materials, which need to be vaporized through a chemical route (other than the physical process as by PVD). Therefore, the possible materials are limited and often the formed precursors are hazardous or corrosive (eg., HF and $SiCl_4$), leading also to hazardous or corrosive byproducts. Furthermore, very often the minimum temperature to allow for a compact thin film growth is rather high (significantly higher than that needed during PVD)

The basic principle is the use of chemical reactions in the surface near region (see Figure 4.3). The resulting species condenses on the heated substrate forming a thin deposit film. Over the years, numerous CVD variations have been developed implying different reactor types, gas flow dynamics, reaction zones and heating techniques. It has become an important standard

technique for many materials, first and foremost the synthesis of diamond [46].

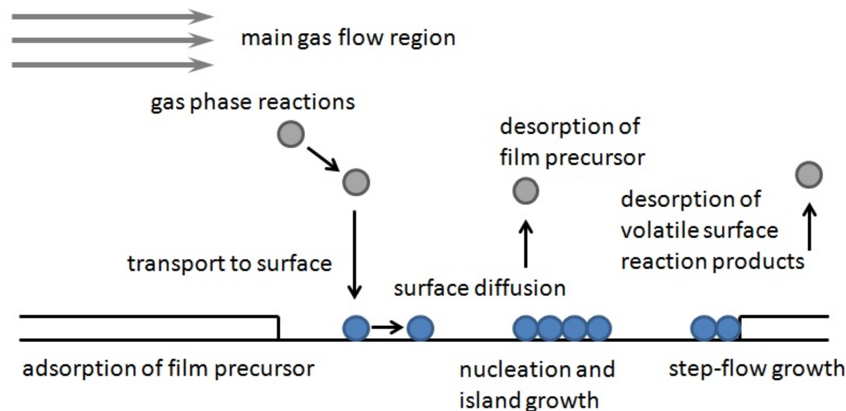

Figure 4.3: Schematics of the CVD process in the surface near region.

4.3 Thin film growth

As already mentioned in the previous sections, the morphology of thin films plays the key role in the range of their properties. To be more specific, the control of grain respectively column size and the crystallinity are the primary concerns in a thin film process. Depending on the homologous temperature (ratio of the substrate temperature to the melting point of the film material), models based on compilations of experimental results have been constructed [47, 48]. These so-called structure zone models (SZM) give important guidelines on the predicted evolution of the structure and have been continuously developed to face divergent requirements. Figure 4.4 illustrates the structure zone model by Anders considering the homologous temperature T^*, the thickness of the film t^* and the logarithmic-scaled normalized energy (E^*). This SZM clearly reveals the expected influence of the different parameters on the morphology of the deposited film. Generally, surface diffusion is the dominating processes in the growth of a thin film [49, 50].

The growth of a thin film is a very complex phenomenon and is characterized by different consecutive stages such as nucleation, island growth, coalescence of islands, the formation of polycrystalline islands and the continuous structure and thickness growth. The formation of the film starts with the primary nucleation on the substrate respectively the secondary nucleation later, developing a liquid like coalescence. In the case of an amorphous substrate, the nuclei are randomly oriented. The fundamental structure forming phenomenon is the crystal growth. As illustrated in Figure 4.5, there are three primary modes of film growth on substrates. The three dimensional growth, also called the Volmer-Weber island growth forms 3D islands into continuous films out from stable clusters. These mechanism occurs

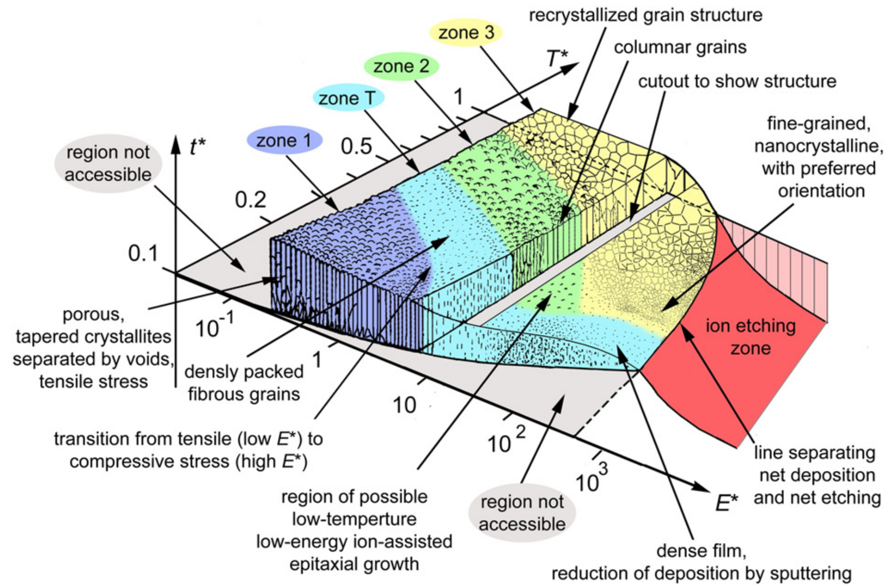

Figure 4.4: Structure zone diagram by Anders [51].

when the adding atoms are more strongly bonded to each other as to the substrates which often appears when forming a metal film on an insulating substrate. If the adding atoms are weaker bonded to each other than to the substrate, the resulting mechanism is the 2D Frank van der Merwe or layer by layer film growth. The third mode is a combination of the previous two. After initially forming a few monolayers, the next layer growth becomes energetically unfavorable and gets compensated by three dimensional island growth. This mechanism is called the Stranski-Kastranow mechanism [6].

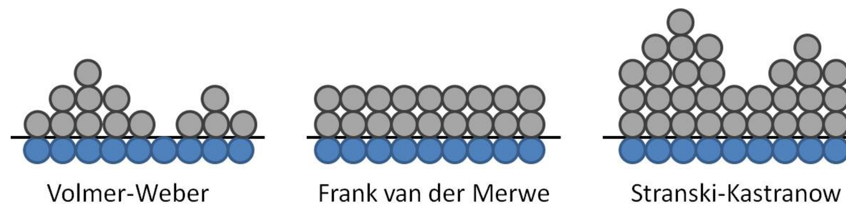

Figure 4.5: Schematics of growth mechanisms for thin films.

Chapter 5

Analysis

To study various structural, mechanical, thermal and electrical properties and characteristics of thin films, the following section will give an overview of the analytical methods used in this study.

5.1 X-Ray Diffraction (XRD)

X-ray diffraction analysis is a powerful instrument for non-destructive determination of structural information of solid matter. Besides the high instrument-based effort, XRD measurements are a fast method of getting information on the existing phases, the grain sizes, textures, stresses and further properties of a solid sample. The principle of XRD is based on the phenomenon of diffraction of electromagnetic waves on periodic structures. This phenomenon occurs assuming that the wavelength of the electromagnetic wave is in the same dimension as the distances of atoms in a crystal lattice (which happens to be fulfilled when using xray radiation). The scattered X-rays can either interfere constructive or destructive. If the conditions satisfy Bragg's law of diffraction (see equation 5.1) the interference is constructive and the diffracted X-rays can be detected and processed. [52]

$$n\lambda = 2dsin\theta \tag{5.1}$$

In this equation n is any integer, λ is the wavelength of the incident beam, d is the spacing between the diffracting planes (lattice plane distances) and θ is the incident angle. Figure 5.1 illustrates Bragg's law of diffraction.

5.2 Hardness measurement - Nanointentation

The scientific term of hardness is defined as the resistance of solid matter to a permanent change of shape (plastic deformation) when a localized compressive force is applied. One of

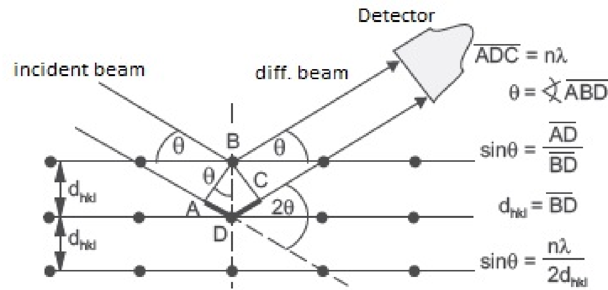

Figure 5.1: Diffraction of monochromatic X-rays on lattice planes.

the earliest hardness tests by Friedrich Mohs (1822) was based on natural occurring minerals with a scale on the ability of one material to scratch another one that was softer. This arbitrary hardness scale ranged from 1 on the soft end (talc) to 10 for the very hard end (diamond). Over the years more quantitative hardness measurement methods (Brinell, Vickers, Knoop, etc.) have been developed in which a small indenter (of various size and shape) is forced into solid matter under controlled load and conditions. Whatever measurement technique is used, one should always be aware that measured hardness values are of relative nature and can only be compared within one technique [53, 54].
Due to the fact that the penetration depth of conventional hardness measurements exceeds the thickness of thin films, Nanointendation becomes the method of choice. This method measures the hardness and the elastic modulus of a material using the load-displacement data (see Figure 5.2) recorded during one cycle of loading and unloading. Therefore, it applies a load on an indenter of defined shape (mostly a Berkowich-diamond) on a sample and evaluates the residual imprint. Through the shape and the penetration depth, the area of contact can be determined. Consequently, the hardness can be determined by the ration of the applied load and the area of contact. Furthermore, knowing the poisson ratio and the indentation modulus of the intender, the reduced elastic modulus can be calculated. To minimize the influence of the substrate, even with nanointendation the penetration depth should not exceed 1/10th of the layer thickness (Empirical law by Bueckle).

5.3 Scanning Electron Microscopy (SEM)

In materials science the scanning electron microscopy has become the most important technique for imaging of thin films. From the cross-sectional view, it provides morphology data and can be used to measure the layer thickness. Furthermore, it can be used to get information on the surface conditions. In the majority of cases it is combined with an energy dispersive detection, which gives additional information on the composition of the sample.

Instead of using visible light, the electron microscope uses a focused electron beam for

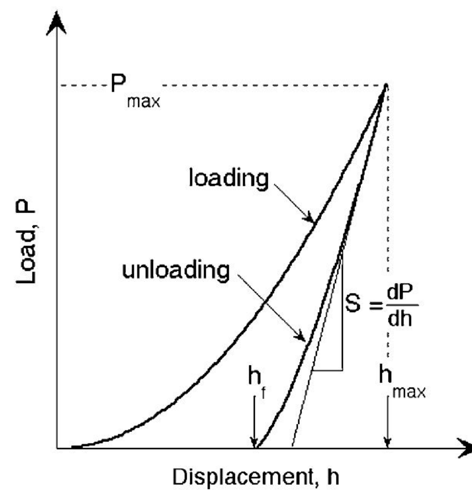

Figure 5.2: Load-Displacement relation [55].

imaging of the sample. According to the Abbe limit, this provides a higher spatial resolution as in optical microscopes. The primary electron beam interacts with the electronic structure of the sample atoms, which leads to elastic and inelastic scattering. These interactions results in the reflection of primary electrons, the so called back scattered electrons (BSE), emission of secondary electrons (SE), auger electrons (AE) and the emission of element specific electromagnetic radiation each of which can be detected separately. By scanning the sample with the focused electron beam the specific signals are detected and an image can be created. Figure 5.3 illustrates the corresponding information (according to their generation depth) of interactions taking place, within the excited volume [56].

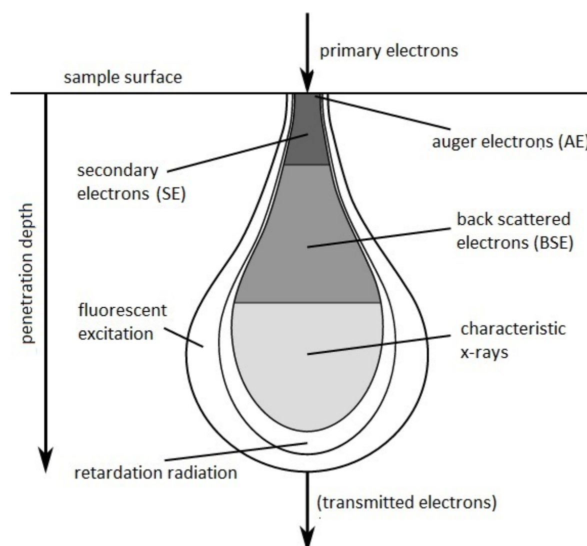

Figure 5.3: Pear-shaped volume of electrons interaction.

5.4 Profilometer

To study surface conditions of thin films, profilometers, which measure the specific height of a specimen, are used. In this case an optical profilometer was used. The technique operates with a white light source, which has a high degree of aberration. The lenses' refractive index is able to vary the focal distance of each wavelength contained in the white light. Hence, each separate wavelength focuses at a different distance from the source, creating the measurement range. When the surface of a specimen is in the range, a single wavelength is in focus while all the others are not. The white light is reflected and after a filter, which separates the light in its wavelengths it gets detected by a charged-coupled device spectrometer (CCD). This technique allows a very high accuracy. [57]

The profilometer can also be used for determining the residual stress occurring in thin films on a given substrate. Therefor, the resulting curvature of a specimen (see Figure 5.4) is determined. Using the stoney equation (see Eq. 5.2 and 5.3) the residual stress can be calculated by knowing the elastic properties of the substrate which are given through the Young's modulus (E) and Poissoin's ratio (ν) [58].

$$\sigma = \frac{E_{substrate}}{(1-\nu_{substrate})} \frac{d^2_{substrate}}{6rd_{film}} \tag{5.2}$$

$$r = \frac{L^2}{8\delta} \tag{5.3}$$

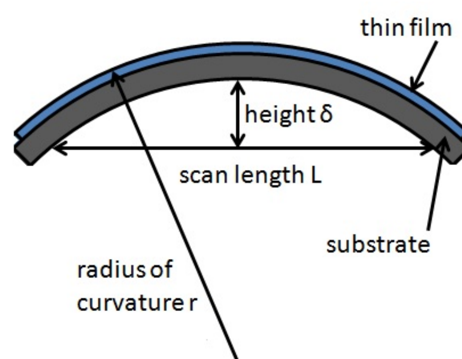

Figure 5.4: Schematics of the specimen due to compressive stressess.

Bibliography

[1] G. A. Slack, R. Tanzilli, R. Pohl, and J. Vandersande, J. Phys. Chem. Solids **48**, 641 (1987).

[2] R. Rachbauer, J. J. Gengler, A. a. Voevodin, K. Resch, and P. H. Mayrhofer, Acta Mater. **60**, 2091 (2012).

[3] H. R. Shanks, P. D. Maycock, P. H. Sidles, and G. C. Danielson, Phys. Rev. **130**, 1743 (1963).

[4] S. Kalpakjian, S. Steven R., and W. Ewald, *Werkstofftechnik - Herstellung, Verarbeitung , Fertigung*, 5th ed. (Pearson Deutschland GmbH, 2011).

[5] C. Yip-Wah, *Introduction to materials science and engineering* (CRC Press, 2007).

[6] P. Martin, *Handbook of Deposition Technologies for Films and Coatings* (Elsevier, 2009).

[7] J. Martan and P. Beneš, Thermochim. Acta **539**, 51 (2012).

[8] F. Rovere and P. H. Mayrhofer, J. Vac. Sci. Technol. A Vacuum, Surfaces, Film. **25**, 1336 (2007).

[9] C. L. Tien and G. Chen, J. Heat Transfer **116**, 799 (1994).

[10] K. Naruse, T. Kawamata, M. Ohno, Y. Matsuoka, K. Kumagai, and Y. Koike, Solid State Commun. **154**, 60 (2013).

[11] T. M. Tritt, ed., *THERMAL CONDUCTIVITY: Theory, Properties, and Applications* (Kluwer Academic / Plenum Publishers, 2004).

[12] R. E. Hummel, *Electronic properties of materials*, fourth edition ed. (Springer Science+Business Media, 2011).

[13] M. J. Graf, S. K. Yip, J. a. Sauls, and D. Rainer, Phy **53**, 17 (1995), arXiv:9509046 [cond-mat] .

[14] R. C. Weast, *CRC handbook of chemistry and physics* (1986).

[15] S. L. Shinde and J. S. Goela, *High Thermal Conductivity Materials* (Springer S, 2006).

[16] M. Handwerg, R. Mitdank, Z. Galazka, and S. F. Fischer, Semicond. Sci. Technol. **30**, 024006 (2015).

[17] J. E. Graebner, S. Jin, G. W. Kammlott, J. a. Herb, and C. F. Gardinier, Appl. Phys. Lett. **60**, 1576 (1992).

[18] G. Slack, J. Phys. Chem. Solids **34**, 321 (1973).

[19] D. D. L. Chung, Appl. Therm. Eng. **21**, 1593 (2001).

[20] E. Riedel and C. Janiak, *Anorganische Chemie* (De Gruyter, 2007).

[21] H. Sumiya and S. Satoh, Diam. Relat. Mater. **5**, 1359 (1996).

[22] S. a. Kukushkin and a. V. Osipov, J. Phys. D. Appl. Phys. **47**, 313001 (2014).

[23] G. a. Slack, J. Appl. Phys. **35**, 3460 (1964).

[24] "Powder Diffraction File 00-025-1133," (2013).

[25] Q. Xia, H. Xia, and A. L. Ruoff, J. Appl. Phys. **73**, 8198 (1993).

[26] K. F. Cai, D. S. McLachlan, G. Sauti, and E. Mueller, Solid State Sci. **7**, 945 (2005).

[27] S. Strite, J. Vac. Sci. Technol. B Microelectron. Nanom. Struct. **10**, 1237 (1992).

[28] J. E. Graebner and H. Altmann, Diamond **7**, 1589 (1998).

[29] D. Twitchen, C. Pickles, S. Coe, R. Sussmann, and C. Hall, Diam. Relat. Mater. **10**, 731 (2001).

[30] E. Ruffio, D. Saury, and D. Petit, Int. J. Heat Mass Transf. **64**, 1064 (2013).

[31] S.-M. Lee and D. G. Cahill, J. Appl. Phys. **81**, 2590 (1997).

[32] D. G. Cahill, Rev. Sci. Instrum. **61**, 802 (1990).

[33] H. Wang and M. Sen, Int. J. Heat Mass Transf. **52**, 2102 (2009).

[34] T. Borca-Tasciuc, a. R. Kumar, and G. Chen, Rev. Sci. Instrum. **72**, 2139 (2001).

[35] a. Jacquot, B. Lenoir, a. Dauscher, M. Stolzer, and J. Meusel, J. Appl. Phys. **91**, 4733 (2002).

[36] T. Tong and A. Majumdar, Rev. Sci. Instrum. **77**, 104902 (2006).

[37] Z.-X. Zong, Z.-J. Qiu, S.-L. Zhang, R. Streiter, and R. Liu, J. Appl. Phys. **109**, 063502 (2011).

[38] N. Bodenschatz, A. Liemert, S. Schnurr, U. Wiedwald, and P. Ziemann, Rev. Sci. Instrum. **84** (2013).

[39] S. Govorkov, W. Ruderman, M. W. Horn, R. B. Goodman, and M. Rothschild, Rev. Sci. Instrum. **68**, 3828 (1997).

[40] A. Goswami, *Thin Film Fundamentals* (New Age International, 1996).

[41] K. Wasa, *Handbook of Sputter Deposition Technology: Fundamentals and Applications for Functional Thin Films, Nano-materials and MEMS* (2012).

[42] W. D. Westwood, *Sputter deposition (AVS Education Committee book series)* (Education Committee, AVS, 2003).

[43] A. Anders, *Cathodic Arcs* (Springer Science+Business Media, 2008).

[44] D. M. Mattox, *Handbook of Physical Vapor Deposition (PVD) Processing*, 2nd ed. (Elsevier, 2010).

[45] L. B. Freund and S. Suresh, *Thin Film Materials: Stress, Defect Formation and Surface Evolution* (Cambridge University Press, 2004).

[46] J.-H. Park and T. S. Sudarshan, *Chemical Vapor Deposition* (ASM International, 2001).

[47] R. Messier, J. Vac. Sci. Technol. A Vacuum, Surfaces, Film. **2**, 500 (1984).

[48] P. J. Kelly, J. Vac. Sci. Technol. A Vacuum, Surfaces, Film. **16**, 2858 (1998).

[49] P. Barna and M. Adamik, Thin Solid Films **317**, 27 (1998).

[50] I. Petrov, P. B. Barna, L. Hultman, and J. E. Greene, J. Vac. Sci. Technol. A Vacuum, Surfaces, Film. **21**, S117 (2003).

[51] A. Anders, Thin Solid Films **518**, 4087 (2010).

[52] L. Spieß, G. Teichert, R. Schwarzer, H. Behnken, and C. Genzel, *Mod. Röntgenbeugung* (Vieweg+Teubner, 2009) pp. 5–40.

[53] W. D. Callister and D. G. Rethwisch, *Fundamentals of Materials Science and Engineering: An Integrated Approach*, 3rd ed. (John Wiley & Sons, 2011).

[54] K. Hermann, *Härteprüfung an Metallen und Kunststoffen: Grundlagen und Überblick zu modernen Verfahren* (expert, 2007).

[55] W. Oliver and G. Pharr, J. Mater. Res. **19**, 3 (2004).

[56] J. Goldstein, *Scanning Electron Microscopy and X-ray Microanalysis: Third Edition*, 3rd ed. (Springer, 2003).

[57] "http://www.nanovea.com/chromatic-confocal.html, 07th feb 2015," .

[58] G. C. a. M. Janssen, M. M. Abdalla, F. van Keulen, B. R. Pujada, and B. van Venrooy, Thin Solid Films **517**, 1858 (2009).

Publication I

Thermal conductivity of nitride based thin films

V. Moraes, H. Riedl, R. Rachbauer, S. Kolozsvári, M.Ikeda, and P.H. Mayrhofer

Manuscript in final preparation.

Thermal conductivity of nitride based thin films

V. Moraes,[1,*] H. Riedl,[1] R. Rachbauer,[2] S. Kolozsvári,[3] M. Ikeda,[4] and P.H. Mayrhofer[1,5]

[1] *Christian Doppler Laboratory for Application Oriented Coating Development at the Vienna University of Technology, A-1040 Wien, Austria*
[2] *Oerlikon Balzers Surface Solutions AG, FL-9496 Balzers, Liechtenstein*
[3] *Plansee Composite Materials GmbH, D-86983 Lechbruck am See, Germany*
[4] *Institute of Solid State Physics, Vienna University of Technology, A-1040 Wien, Austria*
[5] *Institute of Materials Science and Technology, Vienna University of Technology, A-1040 Wien, Austria*

(Dated: March 31, 2015)

The thermal management of various applications including thin films becomes more and more essential. Therefore, the thermal conductivity of these thin films is essential as well as their dependence on structure and alloying content. Based on the 3ω-method, we show the influence of Al and Cr on the temperature dependent thermal conductivity of TiN and, AlN thin films, respectively, and compare them with the results obtained for CrN thin films. The dc sputtered AlN thin films revealed a highly c-axis oriented growth for deposition temperatures of 250 to 700 °C. Their thermal conductivity is beyond the maximum value of $\kappa \sim 50\,\mathrm{W \cdot m^{-1} \cdot K^{-1}}$ at room temperature for our 3ω-method measurement set-up (the limitation is mainly based on the available substrates, here we used Si (100) having $\kappa \sim 142.5\,\mathrm{W \cdot m^{-1} \cdot K^{-1}}$). By the substitution of only 10 at.% Al with Cr, the single-phase wurtzite structure is remained, but κ significantly reduces to $\sim 5\,\mathrm{W \cdot m^{-1} \cdot K^{-1}}$. The single-phase face centered cubic TiN and $Ti_{0.36}Al_{0.64}N$ thin films exhibit κ values of $3.1\,\mathrm{W \cdot m^{-1} \cdot K^{-1}}$ and $2.5\,\mathrm{W \cdot m^{-1} \cdot K^{-1}}$ at room temperature. Hence, also here, the additional element reduces the thermal conductivity, although at a significantly lower level. Single-phase face centered cubic CrN thin films show κ values of $3.6\,\mathrm{W \cdot m^{-1} \cdot K^{-1}}$. For all nitride based thin films investigated, the thermal conductivity slightly increases with increasing temperature between 200 and 330 K. This rather unusual behavior is based on the high defect density (especially point defects) within the thin films prepared by physical vapor deposition.

Keywords: Thermal conductivity; Nitride based thin films; Alloying effects; 3ω method

I. INTRODUCTION

The rapidly growing development of nitride based thin films has led to a great variety of applications. In addition to the very important field of protective coatings for the machining and forming industry or protective coatings for aerospace applications, nitrides are increasingly important for their specific (semi-) conducting and piezoelectric properties, but also for their specific thermal properties. For example, wurtzite (B4) aluminum nitride thin films, a representative of the III-V semiconductors, have drawn great attention over the last decades due to their extremely high thermal conductivity combined with a rather low electrical conductivity (band gap of about 6 eV). The additional excellent thermal stability and high mechanical properties of AlN are extremely attractive combinations for highly sophisticated applications, like functional thin films that also need to withstand friction and wear [1, 2]. AlN is also an ideal candidate for surface acoustic wave devices, due to the outstanding optical and piezoelectric properties combined with a high acoustic velocity of up to $6000\,\mathrm{m \cdot s^{-1}}$ [3, 4].

Face centered cubic titanium and chromium nitride based coatings, which are famous for their wear resistance, diffusion barrier abilities, and tribological properties, are examples of nitrides with a rather low thermal conductivity with $\kappa \sim 4.8\,\mathrm{W \cdot m^{-1} \cdot K^{-1}}$ [5, 6]. These material combinations are ideal for the application as protective hard coatings in forming and tooling industry, leading to the great success of these coatings in these areas. Moreover, TiN thin films are used in solar cells, as high temperature diffusion barriers and shottky or ohmic contact layers in microelectronic devices [7]. $Ti_{1-x}Al_xN$ coatings, which are favored in milling operations, exhibit a pronounced change in mechanical as well as electrical and thermal properties upon annealing treatments (or during exposure to higher temperatures during application) because the single-phase face centered cubic (c) structure decomposes towards the stable constituents c-TiN and wurtzite structured (w) AlN [8].

The thermal conductivity of single crystal w-AlN strongly depends on the oxygen content, grain size, and crystal orientation, and can be as high as $320\,\mathrm{W \cdot m^{-1} \cdot K^{-1}}$ [9]. Especially the crystal structure of AlN (hexagonal wurtzite or cubic zinc blend or face centered cubic rock salt) plays a major role in determining the thermal conductivity due to the primarily responsible heat conduction mechanism, the phonons. Four requirements are needed to obtain a high thermal conductivity: low atomic mass, strong bonding, simple crystal structure, and a low inharmonic behavior [10]. Furthermore, various studies clearly show, that the growth techniques,

* vincent.moraes@tuwien.ac.at

the synthesis conditions, and the substrates used have a strong influence on the microstructure, the crystalline quality of the nitride coatings and thus also on the derived mechanical and thermal properties [11–13]. Therefore, the reported values on the thermal conductivity of AlN thin films cover a tremendously huge range from $\kappa \sim$ 5 to 200 $W \cdot m^{-1} \cdot K^{-1}$ [14–17].

As the thermal conductivity is strongly influenced by the crystal structure, we need to mention that especially the crystal structure of various nitrides can be designed and modified by knowledge-based alloying with various elements, please see for example the ab-initio as well as experimental studies reported in [18, 19].

The thermal conductivity can be obtained by several measurement techniques [20], where the 3ω-method overcomes the difficulties of black body radiation, can be extended for measurements at different temperatures, and counts to the most reliable and accurate techniques [21, 22]. Therefore, this technique was the choice of investigation in our studies.

For a detailed study on the influence of crystal structure, morphology, alloying effect, and deposition conditions on the thermal conductivity (obtained by the 3ω-method in the temperature range 200 K to 330 K) of nitride coatings, we used the single-phase model systems: w-AlN, w-$Al_{0.90}Cr_{0.10}N$, face centered cubic c-CrN, c-TiN, and c-$Ti_{0.36}Al_{0.64}N$.

II. EXPERIMENTAL

All AlN, $Al_{1-x}Cr_xN$, CrN, TiN, and $Ti_{1-x}Al_xN$ thin films were prepared by reactive magnetron sputtering (AJA Orion 5 laboratory-scaled PVD) using a mixed Ar/N_2 glow discharge at a working pressure of 0.4 Pa (both gases with 99.999% purity). Prior to the depositions, the 100-oriented Si substrates (20x7x0.38 mm^3, 10x10x0.38 mm^3) were ultrasonically pre-cleaned in acetone and ethanol, and dc plasma-etched in a pure argon atmosphere at 6.0 Pa for 10 min. To minimize the effect of impurities, the deposition chamber was always evacuated to a base pressure of ≤ 0.9 mPa. To guarantee for a uniform morphology, structure, and chemical compositions of the coatings, the substrate-holder (6 inch diameter) rotated with a frequency of 1 Hz during all depositions.

The aluminum nitride thin films are prepared by powering the 3 inch aluminum target (Plansee Composite Materials GmbH, 99.99% purity) with 11 $W \cdot cm^{-2}$ in dc mode and using an Ar/N_2 flow-rate ratio of 1/9. Eight different AlN thin films are prepared by varying the substrate temperature (T_{dep}= 250, 400, 500, 600, 700, or 800 °C) and the bias potential (floating for all temperatures and −75 V for T_{dep}=250 and 500 °C). Additionally, the AlN coatings prepared at T_{dep}= 250 and 500 °C (with floating and −75 V dc bias) were grown with three different thicknesses between $\sim$ 190 and 1360 nm. Thus, 17 different AlN films were prepared (for more details please see Table I).

The $Al_{1-x}Cr_xN$, CrN, TiN, and $Ti_{1-x}Al_xN$ coatings were only prepared at T_{dep}=500 °C. The $Al_{0.90}Cr_{0.10}N$ coating, 1180 nm thin, is prepared by simultaneous powering the 3 inch aluminum target with 11 $W \cdot cm^{-2}$ and the 2 inch chromium target with 2.5 $W \cdot cm^{-2}$, and using an Ar/N_2 flow-rate ratio of 1/9 with floating potential of the substrates. CrN coatings are prepared with 12.1 $W \cdot cm^{-2}$ dc powering of the 2 inch chromium target (Plansee Composite Materials GmbH, 99.9% purity), an Ar/N_2 flow-rate ratio of 4/6, and −50 V dc bias potential of the substrates, leading to 1070 nm thickness. The TiN coating, 580 nm thickness, is prepared by dc powering the 2 inch titanium target (Plansee Composite Materials GmbH, 99.9% purity) with 12.1 $W \cdot cm^{-2}$ using an Ar/N_2 flow-rate ratio of 8/2 and floating potential of the substrates. The 670 nm thin $Ti_{0.36}Al_{0.64}N$ film is prepared by dc powering the 3 inch $Ti_{0.33}Al_{0.66}N$ compound target (Plansee Composite Materials GmbH, 99.9% purity) with 8.8 $W \cdot cm^{-2}$ in an Ar/N_2 gas mixture (Ar/N_2 flow rate ratio=7/3) and applying −80 V dc bias to the substrates. The details of the deposition conditions are also given in Table I.

TABLE I. Deposition parameters and chemical composition of the thin films prepared by PVD

specimen	T_{dep} [°C]	Bias [V]	Al [at.%]	Ti [at.%]	Cr [at.%]	N [at.%]	thickness [nm]	dep. rate [nm/min]
AlN	250	-	-	-	-	-	200	15.6
AlN	250	-	-	-	-	-	940	15.6
AlN	250	-	-	-	-	-	1320	15.6
AlN	250	-75	-	-	-	-	220	15.5
AlN	250	-75	-	-	-	-	490	15.5
AlN	250	-75	-	-	-	-	910	15.6
AlN	500	-	-	-	-	-	190	16.0
AlN	500	-	44.91	-	-	55.09	1050	16.0
AlN	500	-	-	-	-	-	1360	16.0
AlN	500	-75	-	-	-	-	200	14.9
AlN	500	-75	-	-	-	-	520	14.9
AlN	500	-75	43.31	-	-	56.69	940	14.9
AlN	300	-	-	-	-	-	2190	18.3
AlN	400	-	-	-	-	-	2000	16.7
AlN	600	-	-	-	-	-	1400	11.7
AlN	700	-	-	-	-	-	1340	11.2
AlN	800	-	-	-	-	-	1030	8.6
$Al_{1-x}Cr_xN$	500	-	44.64	-	4.91	50.45	1180	23.6
CrN	500	-50	-	-	50	50	1070	7.6
TiN	500	-	-	38.97	-	61.03	580	5.8
$Ti_{1-x}Al_xN$	500	-80	32.01	17.87	-	50.12	670	22.3

The cross plane (out-of-plane) thermal conductivity was determined with a home-built 3ω-measuring system using a subtraction of the first harmonic wave by an active filter design and operating with the differential technique. The thermal conductivity of the thin films was determined by measuring identical samples with different thicknesses. Detailed descriptions of the setup and technique are reported in [17, 21–23]. The required metal heaters on top of the thin films, for the 3ω method, are prepared by photolithography. Furthermore, electrically

conducting thin films need a non-conducting top-layer prior to the photolithography, to ensure that the electrical current (during the 3ω measurement) is traveling only through the applied metal heaters. Therefore, each specimen, except the AlN thin films, was additionally covered with an $\sim$ 300 nm thin AlN layer. To avoid chemical attack during the photolithography procedure on our nitride based thin films, we used the ion etching technique instead of the less labor-intensive lift off method with KOH based developers [24, 25]. Figure 1 represents a schema of the pre-preparation working sequences of our specimens (AlN top layer on our nitride films with Si-substrate) for the 3ω-measurement. The procedure starts with the sputter deposition of a 5 nm Ti adhesion layer prior to the 75 nm thin Au layer, followed by the covering with a photoresist, the aligning of a photomask, the subsequent exposure to UV-light, and the final preparation of the heaters out of the Ti/Au layer via ion beam etching. Thereby, 75 nm thin Au heaters with a width of 15 μm and a length of 2 mm are prepared on our AlN covered nitride films. The exact dimensions of the individual heaters, which are needed for the exact determination of the thermal conductivity, are obtained by Dektak-profilometer measurements after the preparation steps [26].

The bi-axial stresses within our thin films are calculated via the modified stoney equation using the curvature of the coated Si substrates, obtained by a Nanovea PS50 profilometer [27]. By scanning electron microscopy (SEM, FEI Quanta 200 equipped with a field emission gun) and transmission electron microscopy (TEM, FEI TECNAI F20) of sample cross-sections the growth morphology of our films is studied. Chemical compositions of our films are obtained by energy dispersive X-ray spectroscopy (EDS) with accelerating voltages of 10, 15, and 20 kV.

The structure and phases of our thin films are analyzed by X-ray diffraction (XRD) in Bragg-Brentano configuration (Philips XPERT diffractometer) and in gracing incidence mode (Empyrean Panalytical diffractometer) with a Cu-K$_\alpha$ ($\lambda = 1.54$ Å) radiation source. Our coatings are also characterized for their mechanical properties (hardness (H) and indentation modulus (E)), which are evaluated throughout the loading and unloading segment of the indentation curves (using a UMIS Nanoindenter equipped with a Berkovich tip) according to the Oliver and Pharr method [28].

III. RESULTS AND DISCUSSION

A. Residual stress analysis

Figure 2 clearly shows that with increasing film thickness the stresses change from compression to tensile and that with increasing deposition temperature or bias potential the stresses are more compressive (or less tensile). The AlN thin films exhibit delamination effects

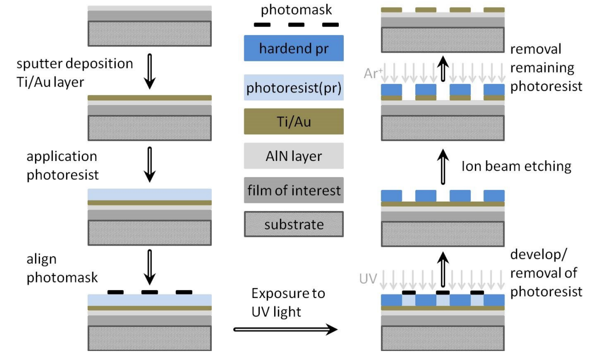

FIG. 1. Working sequence of the photolithography (ion beam etching technique) to microstructure the specimens for the 3ω method.

and micro-crack formation as soon as the tensile stresses are in the range of about 0.5 − 1 GPa, which are typically obtained for thicknesses of $\sim$ 1000 nm. The difference between the thermal expansion coefficient of AlN ($\alpha \sim 4.35 \cdot 10^{-6} \cdot K^{-1}$ at 300 K [29]) and Si substrate ($\alpha \sim 2.69 \cdot 10^{-6} \cdot K^{-1}$ at 336 K [30]) can not explain the increasing compressive stresses (or decreasing tensile stress) with increasing deposition temperature. Increasing the deposition temperature from 250 to 500 °C would lead to thermally induced tensile stresses of about 0.3 GPa (due to the differential thermal expansion coefficient between film and substrate), after cooling down to room temperature.

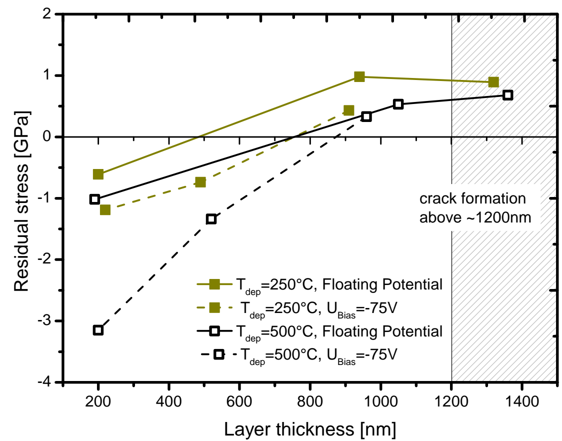

FIG. 2. Residual stress versus obtained coating thickness for various AlN coatings deposited on Si(100). The specimens deposited at 250 and 500 °C are labeled with yellow full symbols and black open symbols, respectively. The applied bias potentials (−75 V/floating potential) are indicated with dashed and solid lines.

Figure 3 shows the stresses re-calculated for the growth temperature, by simply subtracting the thermally induced stresses between deposition and room tempera-

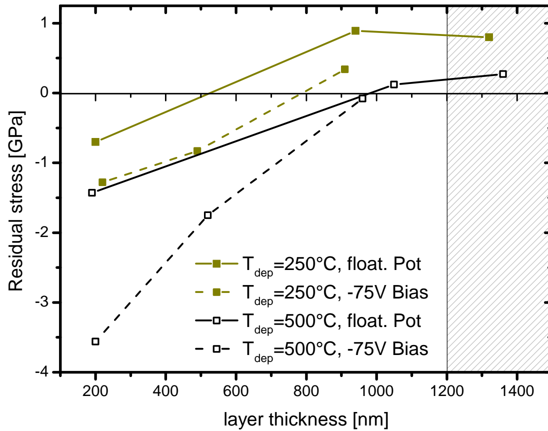

FIG. 3. Re-calculated residual stress (by subtracting the thermally induced stresses) versus obtained coating thickness for various AlN coatings deposited on Si(100).The specimens deposited at 250 and 500 °C are labeled with yellow full symbols and black open symbols, respectively. The applied bias potentials (−75 V/floating potential) are indicated with dashed and solid lines.

ture, where the measurements were performed. Thereby, we can clearly see, that the compressive growth stresses significantly increase with increasing deposition temperature and especially with increasing the bias potential from floating to −75 V. However, the pronounced decrease in compressive stresses with increased layer thickness (in agreement with earlier reports [31]) can not be compensated by the increased deposition temperature or bias potential. But thicker AlN layers (without micro-cracks due to tensile stresses) would be beneficial for the 3ω measurement, because, if the AlN layer is thicker than the high frequency limit of the thermal wave (the geometry of the heater and the thickness of the coating defines the evaluable frequency range), a differential procedure (using AlN layers with different thicknesses) is not needed.

B. Chemistry, structure, and morphology

The chemical composition, obtained by EDS investigations, of our coatings are summarized in Table I. Only for the TiN coating the nitrogen content is not between 50 and 55 at.%, which we attribute to the difficulties of the EDS measuring technique. To simplify notations, all coatings are normalized to 50 at.% nitrogen, and based on the metal sublattice composition of the ternary nitrides we refer to our coatings with AlN, $Al_{0.90}Cr_{0.10}N$, CrN, TiN, and $Ti_{0.36}Al_{0.64}N$.

The XRD patterns of our AlN thin films prepared at various deposition temperatures, Fig. 4, reveal a pronounced c-axis orientation of their wurtzite structure for T_{dep}=250, 400, and 500 °C. The coating prepared at 600 °C already exhibits a more random orientation as also 101 oriented grains can be detected. For the even higher deposition temperatures of 800 °C only an XRD-amorphous structure is obtained and the coating thickness significantly decreases to only 1030 nm suggesting that the high aluminum vapor pressure at the relatively hot substrate surface interferes with the crystal growth (see also the decreasing growth rate for deposition temperatures ≥ 300 °C).

The pronounced c-axis orientation of the w-AlN thin films prepared with deposition temperatures below 600 °C is also the preferable orientation for high thermal conductivity in wurtzite-structured materials [32, 33]. Comparing the XRD pattern obtained in Bragg Brentano mode, Fig. 4, with that obtained in gracing incidence configuration, Fig. 5, suggests that with increasing coating thickness the orientation of the w-AlN film changes to a more random configuration. Within the gracing incidence mode, only the outer most region of the w-AlN thin film contributes to the XRD pattern, whereas in Bragg Brentano mode the entire coating contributes.

By alloying 10 at.% Cr to the metal sublattice of AlN the single-phased wurtzite structure is remained but the orientation becomes even more random, see Fig. 5. Contrary to these two coatings, w-AlN and w-$Al_{0.90}Cr_{0.10}N$, the CrN, TiN, and $Ti_{0.36}Al_{0.64}N$ coatings clearly crystallize with a single-phase cubic structure.

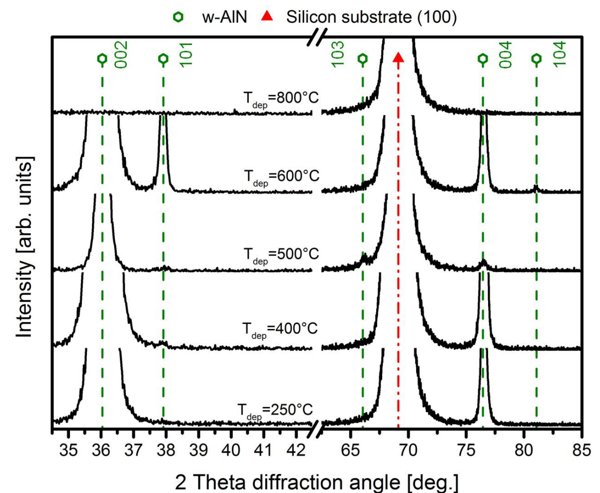

FIG. 4. Structural evolution of the AlN coatings with increasing deposition temperature (T_{dep}=250, 400, 500, 600, and 800 °C). All coatings were deposited with floating bias potential. The 2θ peak positions for standardized w-AlN(a_w=3.11 Å, c_w=4.98 Å [34]) and Si (substrate) are labeled with hexagonal open green symbols and red triangular symbols.

SEM fracture cross sections of the coatings prepared at 500 °C, clearly suggest for a dense growth morphol-

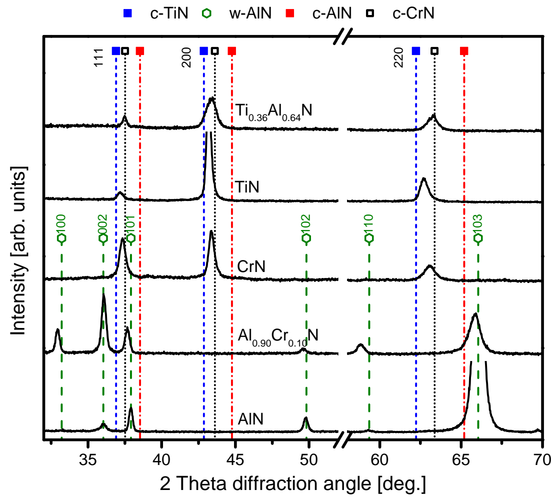

FIG. 5. XRD-patterns (gracing incidence configuration) recorded for AlN, $Al_{0.90}Cr_{0.10}N$, CrN, TiN, and $Ti_{0.36}Al_{0.64}N$ deposited at 500 °C. The AlN coating, 1360 nm thin, is prepared with floating potential. The 2θ peak positions for standardized c-TiN(a_c=4.22 Å [35]), c-CrN(a_c=4.15 Å [36]), c-AlN(a_c=4.05 Å [37]) and w-AlN(a_w=3.11 Å, c_w=4.98 Å [34]) are labeled with solid blue squares, solid red squares, solid black squares, and open green hexagonal symbols.

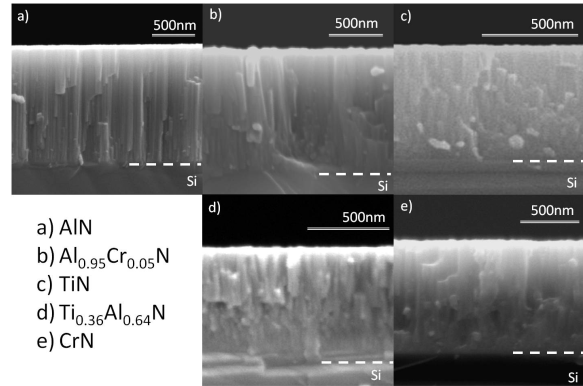

FIG. 6. SEM cross sectional micrographs in the as deposited state of AlN (a), $Al_{0.90}Cr_{0.10}N$ (b), TiN (c), $Ti_{0.36}Al_{0.64}N$ (d), and CrN (e) prepared at T_{dep}=500 °C. The AlN thin film is prepared with floating potential

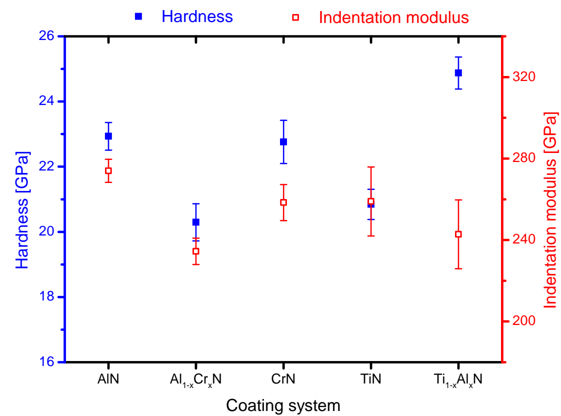

FIG. 7. Hardness (H - blue full symbols) and indentation modulus (E - red open symbols) on Si substrate in the as deposited state of AlN, $Al_{0.90}Cr_{0.10}N$, CrN, TiN, and $Ti_{0.36}Al_{0.64}N$ at T_{dep}=500 °C. The AlN thin film is prepared with floating potential.

ogy and smooth surfaces, see Fig. 6. Especially the smooth surfaces are highly important for accurate 3ω measurements and ideal preparation of the necessary Au-layer heaters. The AlN coating, due to its generally pronounced c-axis orientation, reveals an almost textbook-like columnar growth, Fig. 6a. This slightly changes when alloying with Cr, as thereby also the preferred growth orientation is reduced, Fig. 6b. Contrary, the single-phase cubic structured CrN, TiN, and $Ti_{0.36}Al_{0.64}N$ coatings exhibit a random oriented growth morphology with short columns, see Figs. 6c, d, and e.

C. Mechanical properties

Figure 7 shows the hardnesses and indentation moduli of our single-phase cubic structured CrN, TiN, and $Ti_{0.36}Al_{0.64}N$ coatings in comparison to the single-phase wurtzite structured $Al_{0.90}Cr_{0.10}N$ and AlN coatings, prepared at 500 °C. Here we need to mention that especially the TiN and $Ti_{0.36}Al_{0.64}N$ coatings are rather thin with only 580 and 670 nm, whereas the other coatings are nearly twice as thick with values between 1070 nm and 1360 nm, see also Table I. Consequently, especially the hardness values for TiN and $Ti_{0.36}Al_{0.64}N$ coatings are slightly underestimated. For these two samples, the maximum indentation depth was slightly above 1/10 of the coating thickness. Especially the w-AlN coating prepared at 500 °C with floating potential, which exhibits a pronounced c-axis oriented growth, has with 23.9 GPa a hardness comparable to the single-phase cubic TiN and CrN coatings. By the small addition of only 10 at.% Cr to the metal sublattice the hardness slightly decreases from $\sim$ 23 GPa to 21 GPa, which can be attributed to the change in preferred growth orientation from pronounced 0001 to a more random like, but especially to the composition-induced changes in electronic structure leading to decreasing bulk moduli with increasing Cr content [38].

Our wurtzite structured AlN coatings exhibit comparable hardness and indentation moduli for the different deposition temperatures, see Fig. 8, as long as the preferred orientation is 001 (c-axis oriented). The about 2 GPa difference in hardness between the AlN coatings prepared at 250 °C and 500 °C nearly corresponds to the obtained different compressive stresses for these coatings,

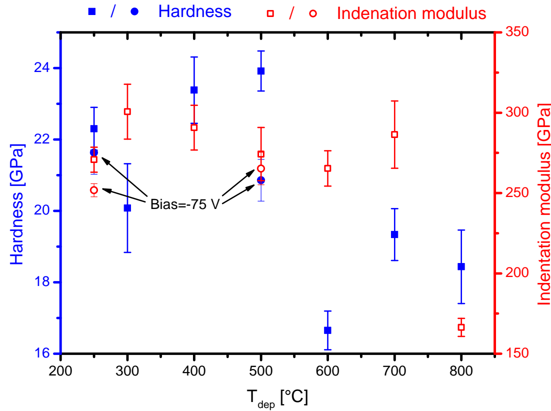

FIG. 8. Hardness (H - blue full symbols) and indentation modulus (E - red open symbols) on Si substrate in the as deposited state of AlN (T_{dep}=250, 300, 400, 500, 600, 700, and 800 °C). The cubic symbols refer to floating potential whereas the round symbols refer to −75 V bias potential.

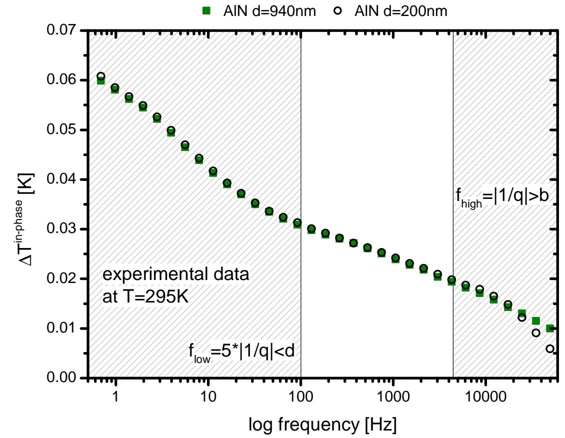

FIG. 9. 3ω measurement on AlN thin film (T_{dep}=250 °C, floating potential) at 295K. The solid green squares and the open black circles are the data points obtained for 940 and 200 nm thin AlN films, respectively.

please compare Figs. 8 and 3. The coatings prepared at 600 °C and 800 °C, which are more random oriented or even exhibit an XRD amorphous structure, exhibit smaller indentation moduli and hardnesses, Fig. 8.

The 001 orientation is the stiffest orientation [39], as can be seen by the indentation moduli for the pronounced 0001-oriented AlN thin film (prepared at T_{dep}=500 °C) with respect to the more random oriented AlN film (prepared at T_{dep}=600 °C) or the XRD-amorphous film (prepared at T_{dep}=800 °C).

D. Thermal conductivity

Figure 9 clearly shows the in-phase [21] temperature drop with increasing heater frequency from 0.1 to ≤ 100 Hz for the measurement at 295 K. The solid green squares and the solid black circles are the data points obtained for 940 and 200 nm thin AlN films, respectively, which were deposited at 250 °C and floating bias potential. The hatched zones covering the frequency ranges below 100 Hz and above 4500 Hz are excluded from the evaluation. In these regions, the thermal wave is either located in the heat sink or in the thin film itself. In the latter case the model of a radial thermal wave for a given heater width (15 μm) is not applicable any more. The empirically obtained low and high frequency boundaries (given in Fig. 9) depend on the thermal wavelength q, the width of the heater b, and the thickness of the coating [21].

Within the useful region (between 100 and 4500 Hz), the data for the 940 and 200 nm thin films are almost identical suggesting for a rather high thermal conductivity of the AlN film. Here we want to mention, that several measurements of various AlN films revealed actually higher thermal barriers for the thinner films than for the thicker ones. The reason for this unexpected behavior could be identified by detailed TEM cross-sectional studies. Thereby, thicker amorphous-like regions near the interface to the Si substrate could be identified for these thinner films exhibiting higher thermal barrier activities. Exemplarily, Fig. 10 shows the cross sectional TEM images for such two significantly different AlN thin films. The amorphous-like layer is about 15 to 20 nm for the thick AlN coating, Fig. 10a, but more than 80 nm for the thinner AlN sample, Fig. 10b. Details of the amorphous regions, by HRTEM investigations, are presented in Figs. 10c and d.

Due to this effect, several specimens, with an unproportional thick amorphous region at the interface, could not be used for the evaluation of our comparable thermal conductivity measurements (differential mode), requiring nearly identical samples with different thicknesses. A rough estimation based on comparable 3ω measurements, yields to a thermal conductivity of $\kappa \sim 25\,\mathrm{W\cdot m^{-1}{\cdot}K^{-1}}$ for the amorphous-like regions. However, this clearly demonstrates the extremely high sensitivity of the used 3ω measurement setup. Pan et al. [17] also reported on the formation of amorphous layers in the interface near region and their effects on the thermal conductivity. Nevertheless, the TEM investigations clearly shows the distinctive dense columns of our AlN coatings.

The measurement data, such as presented in Fig. 9, are fitted with Cahills simulation package [40] to derive the thermal conductivity of the thin films. Figure 11 shows the comparison between the measured and simulated data. When using a thermal conductivity of $10\,\mathrm{W\cdot m^{-1}{\cdot}K^{-1}}$ (blue full/dashed lines), the simulated curve exhibits a significant offset (∼ 0.01 mK for the applied setup) between the 940 and 200 nm thin AlN films. Only for $\kappa \geq 50\,\mathrm{W\cdot m^{-1}{\cdot}K^{-1}}$ (red dotted/dash-dotted line) the simulated curves reveal no significant offset and

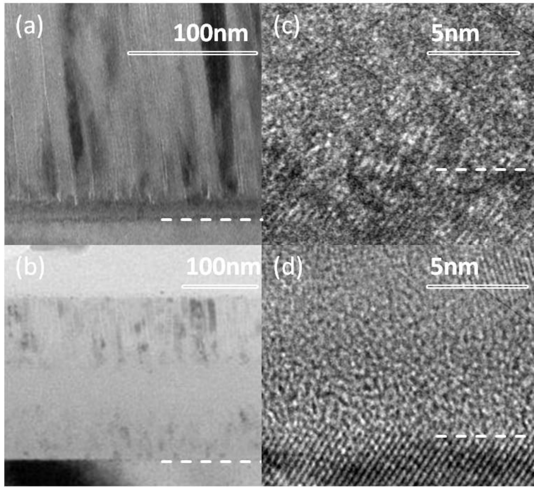

FIG. 10. Cross sectional TEM BF image of (a) thick AlN coating and (b) thin AlN reference sample. High resolution pictures of the interface near regions of both coatings (c) thick AlN coating and (d) thin AlN reference sample. All coatings were deposited at 500 °C with floating potential.

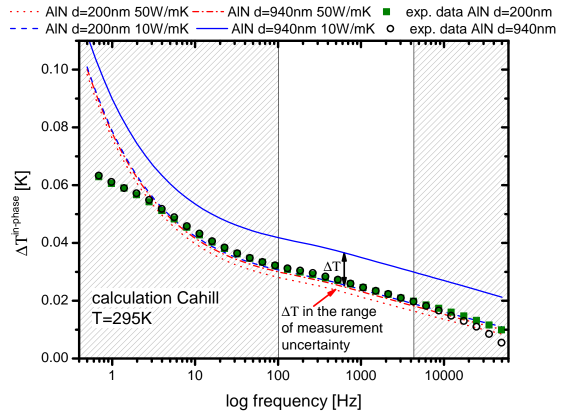

FIG. 11. Simulations of thermal conductivity measurements of AlN thin films applying Cahills package [40]. The solid green squares and the open black circles are the data points obtained for 940 and 200 nm thin AlN films, respectively. Additionally the simulation data for the same setup of films (940 and 200 nm) assuming a thermal conductivity of $10\,\mathrm{W}\cdot\mathrm{m}^{-1}\cdot\mathrm{K}^{-1}$ (blue solid/dashed line) and $50\,\mathrm{W}\cdot\mathrm{m}^{-1}\cdot\mathrm{K}^{-1}$ (red dotted/dash-dotted line) is shown.

correspond to the experimentally obtained data. The error of the measurement, stemming mainly from the errors in size-determination (by profilometry) of the lithographically prepared heaters, is within the range of the used symbol size. However, based on our measurements, which are actually excellently represented by Cahills simulation package (further proofing the high accuracy and feasibility of the 3ω measurement setup used), we can conclude that our w-AlN thin film (prepared at 250 °C and floating bias potential) exhibits a thermal conductivity of $\kappa \geq 50\,\mathrm{W}\cdot\mathrm{m}^{-1}\cdot\mathrm{K}^{-1}$.

The experimental setup is also limited by the substrate used and best results are obtained for thin films with significantly lower thermal conductivity as the substrate. Even if our AlN would exhibit κ values above that of the Si substrate ($\sim 142.5\,\mathrm{W}\cdot\mathrm{m}^{-1}\cdot\mathrm{K}^{-1}$ [41]), the experimentally obtained data points are within the error of the measurement. We have verified this by Cahills simulation. Consequently, we can only give a minimum value for the thermal conductivity of our w-AlN thin films.

The thermal conductivity, obtained with our 3ω measurement setup, could clearly be determined for the other single-phase thin films, w-$Al_{0.90}Cr_{0.10}N$, c-CrN, c-TiN, and c-$Ti_{0.36}Al_{0.64}N$ due to their way lower κ values. Figure 12 shows their data, obtained between 200 and 330 K in steps of 5 K. Especially the binary coatings, c-TiN and c-CrN, exhibit a nearly linear increase of κ with increasing temperature, with a nearly similar slope. The ternary coatings, c-$Ti_{0.36}Al_{0.64}N$ and w-$Al_{0.90}Cr_{0.10}N$, also show an increase in κ with temperature, but with a slightly different slope and offset from linearity. However, both ternaries have lower thermal conductivity than their binary counterparts, c-TiN and w-AlN, respectively. The additional species at the metallic sublattice have serious impact on the phonon-mobility, which are the major carrier of the heat, especially in electrically non-conducting materials. Therefore, the w-$Al_{0.90}Cr_{0.10}N$ thin film, although still single-phase wurtzite structured, exhibits a significantly lower thermal conductivity (with $\kappa \sim 5\,\mathrm{W}\cdot\mathrm{m}^{-1}\cdot\mathrm{K}^{-1}$ at room temperature) than its binary single-phase w-AlN counterpart ($\kappa \geq 50\,\mathrm{W}\cdot\mathrm{m}^{-1}\cdot\mathrm{K}^{-1}$).

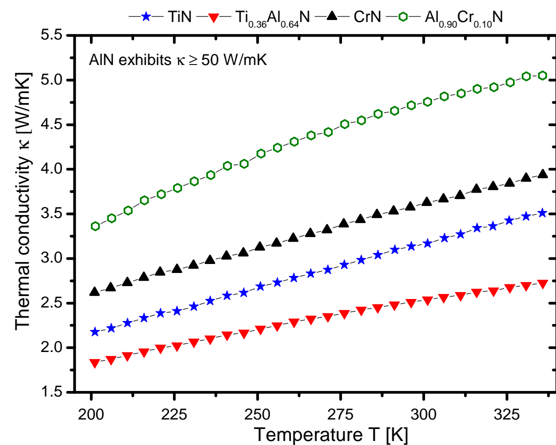

FIG. 12. Thermal conductivity of $Al_{0.90}Cr_{0.10}N$, CrN, TiN, and $Ti_{0.36}Al_{0.64}N$ from 200 to 330 K.

The results clearly show, that the thermal conductivity of single-phase wurtzite structured AlN thin films can significantly be influenced by alloying with Cr. Thereby, values even close to the range of single-phase cubic structured nitride films (in our case c-

TiN and c-CrN) can be obtained. The room temperature (295K) thermal conductivities of our nitride based coatings are: $3.1\,\mathrm{W\cdot m^{-1}\cdot K^{-1}}$ for c-TiN, $2.5\,\mathrm{W\cdot m^{-1}\cdot K^{-1}}$ for c-$Ti_{0.36}Al_{0.64}N$, $3.6\,\mathrm{W\cdot m^{-1}\cdot K^{-1}}$ for CrN, and $4.7\,\mathrm{W\cdot m^{-1}\cdot K^{-1}}$ for w-$Al_{0.90}Cr_{0.10}N$ and are in good agreement with other literature reports on c-TiN and c-CrN [7, 42, 43].

For all nitride based thin films investigated, the thermal conductivity slightly increases with increasing temperature between 200 and 330 K. This rather unusual behavior is based on the high defect density (especially point defects) within the thin films prepared by physical vapor deposition. Calculations proofed, that considering the phonon scattering at point defects as the dominant part of the thermal conductivity leads to an increase in κ with temperature [44].

IV. CONCLUSIONS

In this work, AlN, $Al_{0.90}Cr_{0.10}N$, CrN, TiN, and $Ti_{0.36}Al_{0.64}N$ thin films were deposited on 100-oriented silicon substrates using a dc reactive magnetron sputtering system. In order to explore the thermal conductivity over a wide temperature range, the 3ω-method in the differential operation mode was used.
All thin films studied, revealed dense microstructures with very smooth surfaces. The thermal conductivity of AlN thin films exceeded the measurement setup used. Hence, we can only give a minimum value of $\kappa \sim 50\,\mathrm{W\cdot m^{-1}\cdot K^{-1}}$ for the whole temperature range. Detailed HRTEM cross sections on several AlN thin films revealed that the thicker the amorphous region, at the interface to the silicon substrate, the smaller is the thermal conductivity. These experiments further proof the high accuracy of the 3ω measurement setup used. By alloying 10 at.% chromium to the metal sublattice of the AlN thin film, the thermal conductivity decreases to $5\,\mathrm{W\cdot m^{-1}\cdot K^{-1}}$, while still keeping the preferable single-phase wurtzite structure. TiN thin films exhibited a thermal conductivity of $3.1\,\mathrm{W\cdot m^{-1}\cdot K^{-1}}$ at room temperature. Alloying with $\sim$ 64 at.% of Al further reduces the thermal conductivity to $2.5\,\mathrm{W\cdot m^{-1}\cdot K^{-1}}$.

The results obtained, clearly highlight the enormous potential of physical vapor deposition in independently modifying structure and chemistry of nitride thin films to design their thermal conductivity over a very wide range.

ACKNOWLEDGEMENTS

The authors greatly acknowledge the financial support of Plansee Composite Materials GmbH, Oerlikon Balzers Surface Solutions AG and the Christian Doppler Gesellschaft within the framework of the Christian Doppler Laboratory for Application Oriented Coating Development. SEM investigations were carried out using facilities at the Vienna University of Technology, Austria. Thanks are also due to the X-ray center (XRC) of Vienna University of Technology, Austria.

[1] S. Strite, J. Vac. Sci. Technol. B Microelectron. Nanom. Struct. **10**, 1237 (1992).
[2] P. H. Mayrhofer, C. Mitterer, L. Hultman, and H. Clemens, Prog. Mater. Sci. **51**, 1032 (2006).
[3] M. El Hakiki, O. Elmazria, M. Assouar, V. Mortet, A. Talbi, and F. Sarry, Ultrason **00**, 195 (2004).
[4] H. Loebl, C. Metzmacher, R. Milsom, P. Lok, F. van Straten, and a. Tuinhout, J. Electroceramics **12**, 109 (2004).
[5] J. Martan and P. Beneš, Thermochim. Acta **539**, 51 (2012).
[6] P. H. M. Böttger, L. Braginsky, V. Shklover, E. Lewin, J. Patscheider, D. G. Cahill, and M. Sobiech, J. Appl. Phys. **116** (2014), 10.1063/1.4886182.
[7] A. Albert Irudayaraj, R. Srinivasan, P. Kuppusami, E. Mohandas, S. Kalainathan, and K. Ramachandran, J. Mater. Sci. **43**, 1114 (2008).
[8] R. Rachbauer, S. Massl, E. Stergar, D. Holec, D. Kiener, J. Keckes, J. Patscheider, M. Stiefel, H. Leitner, and P. H. Mayrhofer, J. Appl. Phys. **110** (2011), 10.1063/1.3610451.
[9] G. A. Slack, R. Tanzilli, R. Pohl, and J. Vandersande, J. Phys. Chem. Solids **48**, 641 (1987).
[10] G. Slack, J. Phys. Chem. Solids (1972).
[11] C. C. Wang, C. J. Lu, M. H. Shiao, and F. S. Shieu, J. Vac. Sci. Technol. A Vacuum, Surfaces, Film. **23**, 621 (2005).
[12] T. Aubert, M. B. Assouar, O. Legrani, O. Elmazria, C. Tiusan, and S. Robert, J. Vac. Sci. Technol. A Vacuum, Surfaces, Film. **29**, 021010 (2011).
[13] A. Khanna and D. G. Bhat, J. Vac. Sci. Technol. A Vacuum, Surfaces, Film. **25**, 557 (2007).
[14] B. E. Belkerk, a. Soussou, M. Carette, M. a. Djouadi, and Y. Scudeller, Appl. Phys. Lett. **101**, 1 (2012).
[15] M.-H. Park and S.-H. Kim, Mater. Sci. Semicond. Process. **15**, 6 (2012).
[16] B. E. Belkerk, S. Bensalem, A. Soussou, M. Carette, H. A. Brithen, M. A. Djouadi, and Y. Scudeller, Appl. Phys. Lett. **221905** (2014), 10.1063/1.4903220.
[17] T. S. Pan, Y. Zhang, J. Huang, B. Zeng, D. H. Hong, S. L. Wang, H. Z. Zeng, M. Gao, W. Huang, and Y. Lin, J. Appl. Phys. **112**, 1 (2012).
[18] F. Rovere and P. H. Mayrhofer, J. Vac. Sci. Technol. A Vacuum, Surfaces, Film. **25**, 1336 (2007).
[19] D. Holec, L. Zhou, R. Rachbauer, and P. H. Mayrhofer, J. Appl. Phys. **113** (2013), 10.1063/1.4795590, arXiv:arXiv:1212.4052v2.

[20] J. E. Graebner and H. Altmann, Diam. Relat. Mater. **7**, 1589 (1998).
[21] D. G. Cahill, Rev. Sci. Instrum. **61**, 802 (1990).
[22] T. Borca-Tasciuc, a. R. Kumar, and G. Chen, Rev. Sci. Instrum. **72**, 2139 (2001).
[23] H. Wang and M. Sen, Int. J. Heat Mass Transf. **52**, 2102 (2009).
[24] D. Zhuang and J. H. Edgar, Mater. Sci. Eng. R Reports **48**, 1 (2005).
[25] G. R. Kline and K. M. Lakin, Appl. Phys. Lett. **43**, 750 (1983).
[26] *Dektak 150 Profilometer Instructions*.
[27] G. C. a. M. Janssen, M. M. Abdalla, F. van Keulen, B. R. Pujada, and B. van Venrooy, Thin Solid Films **517**, 1858 (2009).
[28] W. Oliver and G. Pharr, J. Mater. Res. **19**, 3 (2004).
[29] H. Iwanaga, a. Kunishige, and S. Takeuchi, J. Mater. Sci. **35**, 2451 (2000).
[30] Y. Okada and Y. Tokumaru, J. Appl. Phys. **56**, 314 (1984).
[31] P. Pobedinskas, J. C. Bolsée, W. Dexters, B. Ruttens, V. Mortet, J. D'Haen, J. V. Manca, and K. Haenen, Thin Solid Films **522**, 180 (2012).
[32] J. E. Graebner, S. Jin, G. W. Kammlott, B. Bacon, L. Seibles, and W. Banholzer, J. Appl. Phys. **71**, 5353 (1992).
[33] J. E. Graebner, S. Jin, G. W. Kammlott, J. a. Herb, and C. F. Gardinier, Nature **359**, 401 (1992).
[34] "Powder Diffraction File 00-025-1133," (2013).
[35] "Powder Diffraction File 04-015-2441," (2014).
[36] "Powder Diffraction File 01-077-0047," (2014).
[37] "Powder Diffraction File 00-046-1200," (2013).
[38] P. H. Mayrhofer, D. Music, T. Reeswinkel, H. G. Fuß, and J. M. Schneider, Acta Mater. **56**, 2469 (2008).
[39] a. F. Wright, J. Appl. Phys. **82**, 2833 (1997).
[40] D. G. Cahill, "http://users.mrl.illinois.edu/cahill/tcdata/tcdata.html," (2009).
[41] H. R. Shanks, P. D. Maycock, P. H. Sidles, and G. C. Danielson, Phys. Rev. **130**, 1743 (1963).
[42] R. Rachbauer, J. J. Gengler, A. a. Voevodin, K. Resch, and P. H. Mayrhofer, Acta Mater. **60**, 2091 (2012).
[43] T. Ibrahim and T. Ghrib, New Tribol. Ways (2011).
[44] "Private communication with Matthias Ikeda, February 2nd, 2015, Vienna University of Technology,".